2019-02-11

Physical and Numerical Modeling of Infragravity Wave Generation and Transformation on Coral Reef Platforms

Masselink, Gerd

http://hdl.handle.net/10026.1/13555

10.1029/2018JC014411
Journal of Geophysical Research: Oceans
American Geophysical Union

3.24RESEARCH ARTICLE
10.1029/2018JC014411

Physical and numerical modelling of infragravity wave generation and transformation on coral reef platforms

Gerd Masselink[1], Megan Tuck[2], Robert McCall[3], Ap van Dongeren[3], Murray Ford[2] and Paul Kench[2]

[1]Coastal Processes Research Group, School of Biological and Marine Sciences, University of Plymouth, Plymouth, UK
[2]School of Environment, University of Auckland, Auckland, New Zealand
[3]Department of Applied Morphodynamics, Unit of Marine and Coastal Systems, Deltares, Delft, Netherlands

Key Points

- Infragravity (IG) wave motion on reef platforms (generation mechanism and energy level) is strongly affected by fore reef slope
- On most natural coral reef systems with steep fore reefs (> 1:20) the breakpoint-forced long wave mechanism of IG generation is dominant
- IG wave height across reef platforms depends on incident wave height, fore reef slope, water depth across the reef and wave period

Correspondence to:
G. Masselink
G.Masselink@plymouth.ac.uk

Citation:
Masselink, G., Tuck, M., McCall, R., van Dongeren, A., Ford, M., Kench, P. (2019), Physical and numerical modelling of infragravity wave generation and transformation on coral reef platforms. *Journal of Geophysical Research: Ocean, 124.* https://doi.org/10.1029/2018JC014411

Received 27 JUL 2018
Accepted 5 FEB 2019
Accepted article online 1 FEB 2019

Abstract Wave transformation across reef platforms strongly controls sediment transport processes and coral reef island morphodynamics with infragravity (IG) waves playing an important contributing role. A small-scale (1:50) laboratory experiment and proto-type numerical modelling are used to explore the characteristics of IG wave motion on coral reefs. The slope of the fore reef is the key factor controlling the mechanism of infragravity wave generation. Steep slopes (> 1/10) are dominated by landward and seaward propagating breakpoint-forced long waves (BFLWs), whereas incoming and then released bound long waves (BLWs) become increasingly important for slopes < 1/20. The BFLW mechanism is the more effective generator of IG energy and the most energetic IG motion (normalised by incident wave motion) is generated on reef platforms with a fore reef slope > 1/6. The water level relative to the reef platform h_{reef} is also a key factor and the largest IG waves are generated for a ratio between h_{reef} and offshore significant wave height $H_{s,o}$ of -0.25 to 0.75, i.e., when most waves break across the reef slope and a fully saturated surf zone extends across the reef platform. An island on the reef platform substantially increases the contribution of IG waves to the total wave spectrum, but increased reef surface roughness reduces IG importance. Under the most optimal conditions, the IG wave height averaged across the platform is 20–30% of the incident offshore wave height. The geomorphic influence of IG waves is considered most significant for reef platforms with energetic waves breaking on the steepest fore reefs.

1. Introduction

Fringing reefs and coral atolls are ubiquitous in the tropical seas and are generally characterized by a steep fore reef, a narrow reef crest region and a sub-horizontal reef platform. The elevation of the reef platform is usually around mean low tide level; therefore, the platform may be emerged at low tide and submerged during high tide (*Young*, 1990; *Beetham et al.*, 2015). Beaches composed of reef-derived carbonate sediments may be present on these reef platforms and, in the case of coral atolls, these beaches may form islands, referred to as 'cay' and 'motu' for sand and gravel islands, respectively (*McLean, 2011; Kench, 2013*). Whether vegetated or unvegetated, reef islands typically have low elevations, rarely rising more than 4 m above reef platform surface (*Smithers*, 2011; *Kench*, 2013), but, despite their limited size and low elevation, reef islands provide the only land for habitation in mid-ocean atoll settings. The accumulation of islands on reef surfaces is controlled by wave and current deposition of carbonate sediments and their shorelines undergo dynamic adjustments to the normal range of changes in incident wave processes *(Kench and Brander*, 2006; *Kench et al.*, 2017). However, the islands are considered vulnerable to extreme storms and water levels on the short time scale (*Hoeke et al.*, 2013; *Quataert et al.*, 2015), and sea-level rise over longer time scales (*Sheppard et al.*, 2005; *Storlazzi et al.*, 2015; 2018; *Beetham et al.*, 2017). Empirical and numerical models are in development to simulate storm processes and sea-level rise on coral reef platforms to assess wave-driven inundation and hazards on reef islands (*Grady et al.*, 2013; *Storlazzi et al.*, 2011, 2015, 2018; *Pearson et al.*, 2017). Ocean waves acting on the reef platform are the key factor for reef island geomorphology and dynamics (*Kench and Brander*, 2006), and these predictive models must, therefore, be based on a thorough quantitative understanding of the wave transformation processes across the reef platforms.

Sediment transport processes across coral reef platforms are governed by hydrodynamic processes operating over a range of time scales. Most of the sediment transport is generated by flows directly or indirectly generated by ocean waves, i.e., wave orbital velocities and nearshore currents, respectively (*Kench*, 1998; *Ogston et al.*, 2004; *Vila-Concejo et al., 2013*). Tidal currents can also play a significant role, especially when channels are present (*Kench and McLean*, 2004), but the main role of the tide is to modulate the ocean-wave processes (*Young*, 1990; *Brander et al.*, 2004). At low tide almost all wave breaking will take place across the fore reef, limiting wave energy on the reef platform, whereas at high tide waves typically break at the reef crest and continue to transform across the reef platform. Wave energy dissipation across the fore reef and the reef platform due to wave breaking is very effective due to the shallow water depths and by the time incident waves reach the shoreline they are very much reduced in height (*Péquignet et al.*, 2011; *Lowe et al.*, 2005). However, breaking-induced energy dissipation across the reef platform generates radiation stress gradients which, in turn, are responsible for elevated water levels in the form of wave set-up (*Gourlay*, 1996a, b; *Jago et al.*, 2007; *Vetter et al., 2010; Becker et al.*, 2014). Wave set-up can be very significant and *Péquignet et al.* (2009) recorded a super-elevated water level across a reef platform in excess of 1 m during storm wave conditions (H_s = 4 m). Such elevated water levels are important in their own right, but the increased water depth due to wave set-up also enables relatively large waves to propagate across the reef platform and, in combination with runup (*Pearson et al.*, 2017), potentially increases the risk of inundation.

In between the tidal water fluctuations operating on a time scale of hours and incident waves at time scales of seconds, infragravity waves or long waves, which represent water fluctuations on a time scale of 30 s to 5 min, are also of importance. Following early work by *Hardy and Young* (1996) and *Lugo-Fernandez et al.* (1998), the role of infragravity waves, henceforth IG waves, to reef platform water-level dynamics has recently been explored in a number of field investigations (*Ford et al.*, 2013; *Péquignet et al.*, 2014; *Beetham et al.*, 2015), laboratory experiments and numerical modelling (*Nwogu and Demirbilek*, 2010; *Torres-Freyermuth et al.*, 2012; *Yao et al.*, 2012; *van Dongeren et al.*, 2013; *Ma et al.*, 2014; *Pomeroy et al.*, 2015; *Shimozono et al.*, 2015). In particular, the field studies of *Péquignet et al.* (2009) and *Pomeroy et al.* (2012) have shown that incident waves and mean nearshore currents accounted for only a small part of the total observed surface elevation and flow variance in the region between the reef crest and the shoreline of two fringing reefs. Instead, the bulk of the water level variability was found to be contained within the IG frequency band. *Cheriton et al.* (2016) also studied wave dynamics on a fringing reef and found that during a storm event with a maximum offshore significant wave height of 6 m and peak wave periods of 16 s, the infragravity wave energy at the shoreline represented a significant wave height in excess of 1 m. Depending on the wave length of the IG waves, the reef platform width and the water depth across platform, resonant wave conditions may prevail that can significantly enhance the energy level of the IG-band water motion (*Gawehn et al.*, 2016), and therefore the potential for coastal inundation and damage (*Roeber and Bricker*, 2015).

Generally, two mechanisms for the generation of IG waves are considered, both related to wave groups. (1) Bound long waves (BLW) are in near anti-phase (180° out of phase) with the wave groups (*Longuett-Higgins and Stewart*, 1962) and as they propagate towards the shoreline in shallow water, energy is transferred from the short waves to the long waves (*Janssen et al.*, 2003). It is commonly assumed that the BLW is released by short-wave breaking and continue to propagate to the shore as a free wave. However, *Baldock* (2012) argues that the BLW reduces in amplitude due to short-wave breaking and will only be released from the wave groups once the waves are in shallow water. (2) Breakpoint-forced long waves (BFLW) are related to the time-varying wave set-up modulated by wave groups (*Symonds et al.*, 1982), causing the wave breakpoint to oscillate at the wave group frequency and act as an IG wave generator. According to the BFLW mechanism two IG waves are generated, both originating at the wave breakpoint: a set-up wave propagating to the shore (in phase with wave groups) and a set-down wave travelling out to sea (in anti-phase with wave groups). Once generated and/or released, these waves can dissipate energy through bed friction (*Henderson and Bowen*, 2002; *de Bakker et al.*, 2014), transfer energy to other frequencies (*Henderson et al.*, 2006; *Inch et al.*, 2017), break (*van Dongeren et al.*, 2007) and/or reflect to set up (partially) standing wave patterns (*Guza and Thornton*, 1985). Field evidence of both IG wave mechanisms has been documented (BLW: *List*, 1991; *Masselink*, 1995; *Inch et al.*, 2017; BFLW: *Pomeroy et al.*, 2012; *Contardo and Symonds*, 2013)

Despite the widely acknowledged importance of IG waves for reef hydrodynamics, there has been limited work to investigate the origin of the IG motion in reef environments. *Baldock* (2012) proposed a useful framework to enable an evaluation of the relative importance of the two mechanism through a surf beat similarity parameter $\xi_{surfbeat}$, which combines the normalised bed slope with the wave steepness:

$$\xi_{surfbeat} = \beta_{norm}\sqrt{\frac{H_b}{L_o}} \quad \textbf{(Eq. 1)}$$

where L_0 is the short-wave deep-water wave length, H_b is the wave height at the breakpoint and β_{norm} is the normalised bed slope as proposed by *Battjes et al.* (2004):

$$\beta_{norm} = \frac{h_x}{\omega_{low}}\sqrt{\frac{g}{h_b}} \quad \textbf{(Eq. 2)}$$

where h_x and h_b are the beach slope and the depth at breaking, respectively, ω_{low} is the radian long-wave frequency, and g is the gravitational acceleration. Small and large values of $\xi_{surfbeat}$ favour the BLW and BFLW mechanism, respectively, with a $\xi_{surfbeat}$ value of 0.05–0.1 separating the two IG wave regimes (*Baldock*, 2012, his Table 1; *Contardo and Symonds*, 2013, their Table 2). Only a few studies have applied this concept to reef environments and this work has suggested that on coral reef environments with their steep fore reefs, the BFLW mechanism is favoured (*Péquignet et al.*, 2009; *Pomeroy et al.*, 2012).

This paper investigates the characteristics of IG wave motion on coral reef platforms using a small-scale (1:50) laboratory experiment complimented by proto-type numerical modelling using the wave-resolving (non-hydrostatic) version of the XBeach model. The physical model results are investigated in their own right, but are also used to help validate the numerical model. XBeach is then used to explore further the relevant parameter space to gain further insights into the generation mechanism and the characteristics of IG wave motion across coral reef platforms. The specific objectives of this research are to: (1) assess the relative importance of the BLW and BFLW mechanism of IG generation of coral reef platforms for different reef morphologies, especially the effect of the foreshore slope; (2) investigate the role of coral reef islands in affecting the IG wave motion across the reef platform; and (3) identify the conditions most conducive for generating energetic IG motion across coral reef platforms.

2. Methodology

The approach followed in this paper is to reproduce in a small-scale laboratory setting, as well as in a numerical model, conditions of a 'real' coral reef platform. The location used here as the proto-type is the uninhabited gravel island (motu) of Fatato, located along the outer rim of the Funafuti atoll, Tuvalu (Figure **1a**). Fatato extends c. 900 m alongshore, with a maximum across-shore width of 90 m (Figure **1b**). The double-ridged island is characterised by a steep and narrow ocean beachface (c. 12°) with an elevated berm (3.5 m above mean sea level), a vegetated central basin (1.5–2.0 m above MSL) and lower elevation lagoon side berm (Figure **1c**). Funafuti is one of the higher elevation atolls in the Pacific and this is attributed to a historic sea-level high stand.

The ocean beach is comprised primarily of pebble-to-cobble size material, while the lagoon shoreline is composed of coarse sand (*Kench et al.*, 2017). Boulder size deposits on the reef flat, beach face and central depression show evidence of historic high energy and wave overtopping events, indicating that storms and/or swell exposure have played an important role in the formation and maintenance of the motu's geomorphology. The ocean reef flat at Fatato is c. 90 m wide and exhibits a range of morphological features. The inner section is characterised by a semi-continuous zone of cemented rubble. Central and outer sections of the reef flat are comprised of smooth reef pavement covered in crustose coralline algae with encrusting corals present on the seaward reef crest. The ocean-facing fore reef at Fatato has a slope of 27° (1:2) and is characterised by a distinct spur and groove system. The leeward (lagoon) reef flat is c. 130 m wide and is relatively smooth and devoid of large morphological features such as boulder deposits.

Funafuti Atoll has a semi-diurnal, predominantly micro-tidal regime (spring tide range = 2.0 m; neap tide range = 0.5 m) and at spring high tide the water level is 1.1 m above MSL. Located on the southeast side of Funafuti, Fatato is exposed to the prevailing easterly trade wind system. The island shoreline is oriented at 143° and is directly exposed to waves approaching between 60° and 214°, with the eastern and southern tips of Funafuti Atoll shadowing direct wave approach from the northeast and southwest (Figure **1a**). Mean incident wave conditions on the eastern rim of Funafuti are characterised by offshore significant wave height $H_{s,o}$ of 1.3 m, significant wave period T_s of 11 s, with a peak direction D_p of 114° (*Bosserelle et al.*, 2016). Larger waves persist through the winter months (June to October) with mean $H_{s,o}$ = 1.5 m, max-monthly $H_{s,o}$ = 2.3 m and mean D_p = 123°. Summer months (November to April) are associated with smaller wave heights (mean $H_{s,o}$ = 1.2 m) that approach the atoll from the east. The largest waves that impact Funafuti are generated by regional tropical cyclone activity (between December and April) that produces significant wave heights of 3–4 m with periods of 10–14 s, and such conditions occur every 3–5 years (*Bosserelle et al.*, 2016).

*Figure **1** here*

2.1. Small-Scale Laboratory Modelling

Experimental tests to study reef platform hydrodynamics were undertaken in the Tilting Flume (length = 20 m; width = 0.6 m; depth = 1 m) at the COAST (Coastal, Ocean and Sediment Transport) lab at the University of Plymouth, UK (https://www.plymouth.ac.uk/research/institutes/marine-institute/coast-laboratory). The laboratory reef platform was constructed to a geometric 1:50 scale and Froude scaling was used to maintain hydrodynamic similitude for a balance between the inertia and gravitational terms (please note that this does not work if bottom drag is dynamically important). The reef platform (8 m long and 0.6 m wide), was constructed out of marine plywood and consisted of a horizontal reef platform resting 0.47 m above the flume floor with a 1:2.3 fore reef and back reef slope measuring 1.13 m long (Figure **2**). Quartz sand of a median sediment size D_{50} of 0.35 mm was glued to the surface of the reef platform and slopes to represent surface roughness ($k_s = 3D_{50} \approx 1$ mm). The reef platform was positioned with the fore reef slope located 9 m from the face of the (absorbing) piston-type wave paddle. For the tests with an island present, the latter was constructed out of medium-size quartz sand (D_{50} = 0.35 mm), representing medium-size gravel at the prototype (D_{50} = 18 mm). The island was shaped using a wooden template with the same cross-shore profile as that surveyed across Fatato (Figure **1c**). The reef island had two ridges, a width of almost 3 m and a maximum height of 8 cm, representing 150 m and 4 m at the prototype.

*Figure **2** here*

Wave transformation across the reef platform without a reef island was measured during Test Series A – C, whereas Test Series E was conducted with the island placed on top of the reef platform (Table **1**). Test Series A – C consisted of 18 x 12-min tests with the reef platform exposed to significant wave heights $H_{s,o}$ of 0.04, 0.06 and 0.08 m, representing $H_{s,o}$ of 2, 3 and 4 m at the prototype, and peak wave periods T_p of 1.4 and 2.3 s, representing T_p of 9.9 and 16.3 s at the prototype. The still water level relative to the reef platform h_{reef} was 0, 0.02 and 0.04 m, representing 0, 1 and 2 m at the prototype, and considered low tide, mid-tide and high tide. All wave conditions were irregular and generated using a JONSWAP wave steering signal specified by H_s and T_p using a peak enhancement factor γ of 3.3 (i.e., narrow-banded spectrum). The water levels across the reef platform were recorded at a frequency of 32 Hz using an across-reef array of 15 capacitance wire wave probes. The capacitance wires were calibrated at the start of each day of testing, and they were zeroed at the start of each wave test.

*Table **1** here*

2.2 Proto-type XBeach modelling

Numerical modelling of the reef platform hydrodynamics was conducted at the proto-type using the phase-resolving (i.e., non-hydrostatic) variant of the widely used and open-source XBeach model (*Roelvink et al.*, 2009; https://oss.deltares.nl/web/xbeach/). XBeach models were set-up in 1D (depth-averaged, cross-shore transect) mode using the GUI provided in XBeach-G, the gravel variant (sediment size > 2 mm) of XBeach (*Masselink et al.*, 2014). The cross-sectional shape of the coral reef platform and reef island was exactly the same as that in the small-scale laboratory experiment, but at the proto-type scale (Figure **2**). Likewise, the modelled wave and water-level conditions were identical to the laboratory conditions, but also at a proto-type scale. The numerical model was run using default parameters of the non-hydrostatic XBeach model and model duration was 83 min.

In addition to replicating the conditions in the laboratory, an additional series of XBeach models was set-up to simulate a typical storm condition ($H_{s,o}$ = 2.5 m; T_p = 12.5 s), but with variable water levels (-6, -4, -2, -1, 0, +1, +2, +4, +6 m) and fore reef gradients (1:1, 1:2, 1:3, 1:4, 1:5, 1:6, 1:7, 1:8, 1:10, 1:15, 1:20). The purpose of these model runs was to extend the parameter space represented by the small-scale laboratory experiment and provide further insights into the relative importance of the different IG wave generation mechanisms. Finally, the numerical model was also used to investigate the IG wave height across the seaward part of the reef platform as a function of wave conditions, water level and fore reef slope. A very large number (c. 4000) of model runs were run with the boundary conditions selected randomly from a realistic range of values. The runs were all set up with a 200-m wide reef platform rising above a water depth of 50 m to ensure that incident waves at the boundary are in relatively intermediate water depths, with no island on the platform, and a relatively gently-sloping (1:10) back-slope leading into an open lagoon to avoid strong reflections. For each model run, the slope of the fore reef was selected randomly between 1/50 and 1/1; the water level h_{reef} was selected randomly between -3m to +3m relative to the level of the reef platform; the offshore wave height H_s was selected randomly between 1 and 6 m, a corresponding peak period T_p was selected based on wave steepness (randomly varying between 0.003 and 0.05), and a uniform bed friction value of c_f = 0.002 was used

2.3 Analysis

For the data analysis, the length of time series analysed was 10 min for the physical model data and 60 min for the numerical modelling data, whereby the first 2 and 23 min, respectively, were considered 'spin-up time' as by the end of this period a quasi-steady wave set-up profile had established. To quantify the incident (INC) and infragravity (IG) wave heights, each water surface elevation time series η_t was separated into $\eta_{t,INC}$ and $\eta_{t,IG}$ using a simple Fourier filter with a frequency cut-off corresponding to a period of $2T_p$. The significant wave height H_s was computed as $H_s = 4\sigma$, where σ is the standard deviation associated with the relevant water surface elevation time series. Wave set-up and set-down across the reef morphology was computed as the mean of η_t.

The generation mechanism of infragravity waves across the reef platform was investigated using cross-correlation analysis between wave groups and IG wave motion following *List* (1986), *Masselink* (1995) and *Pomeroy et al.* (2012). Here, the wave group time series A_t is estimated using *List* (1991), which involves high-pass filtering the data, taking the modulus of the time series and low-pass filtering the data (the final step of multiplying the time series by $\pi/2$ was not carried out). The high-pass filter used was $1/(2T_p)$ Hz, which corresponds to the spectral valley evident in all spectra from outside the breaker zone, but the low-pass filter used was $1/(4T_p)$ Hz as the vast majority of the IG energy in the wave spectra was at frequencies lower than this value and only very limited amounts of energy were present at $1/(4T_p)$ – $1/(2T_p)$ Hz. For the cross-correlation analysis, the time series of the IG wave motion $\eta_{t,IG}$ was obtained by low-pass filtering η_t using the same low-pass filter of $1/(4T_p)$ Hz.

Cross-spectral analysis was performed to investigate the correlation in the frequency domain. The spectra were computed from time series of 19200 points (collected at 32 Hz) for the laboratory data and 4096 points for the numerical model data (collected at 1 Hz) using the segment-averaging or Welch method. The time series were subdivided into 8 non-overlapping, Hanning-tapered segments, resulting in 16 degrees of freedom. The confidence limits of the spectra are related to the degrees of freedom through the Chi-squared distribution (e.g., *Beauchamp and Yuen*, 1979):

$$S(j)\frac{\nu}{\chi^2_{\nu,\alpha/2}} \leq S(j) \leq S(j)\frac{\nu}{\chi^2_{\nu,1-\alpha/2}} \quad \textbf{(Eq. 4)}$$

where $S(j)$ are the spectral estimates and j refers to the frequency index, ν are the degrees of freedom and α is the confidence level. For a significance level of 95% (α = 0.05) and ν = 16, the associated confidence band is [$0.55S(j)$–$2.32S(j)$]. The significance level of the (squared) coherence, K^2_{sig} was determined following *Thompson* (1979) as:

$$K^2_{sig} = 1 - \alpha^{1/(\nu/2)-1} \quad \textbf{(Eq. 5)}$$

which for α = 0.01 and ν = 16 results in K^2_{sig} = 0.48. The confidence limits of the phase are dependent on the coherence, the degrees of freedom and the required confidence level, and were computed using the technique outlined in *Jenkins and Watts* (1968; their Fig. 9.3). As an indication, for 16 degrees of freedom and a coherence of 0.5, the 95% confidence interval for the phase is $\pm 22^{\circ}$.

The IG signal is likely to contain incoming (shoreward-propagating) and outgoing (seaward-propagating) components. The method by *Guza et al.* (1984) is used here to decompose the XBeach modelled infragravity signal into incoming and outgoing components using time series of water surface elevation and cross-shore current velocity and assuming shallow water waves:

$$\eta_{t,IG,in} = \frac{\eta_{t,IG} + u_{t,IG}\sqrt{h/g}}{2} \quad \textbf{(Eq. 6)}$$

$$\eta_{t,IG,out} = \frac{\eta_{t,IG} - u_{t,IG}\sqrt{h/g}}{2} \quad \textbf{(Eq. 7)}$$

where $\eta_{t,IG,in}$ and $\eta_{t,IG,out}$ are the incoming and outgoing IG signals, respectively, $\eta_{t,IG}$ and $u_{t,IG}$ are the low-pass filtered water surface elevation and cross-shore current time series, respectively, h is the mean water depth and g is gravitational acceleration.

3. Results

3.1 Measurements of wave transformation across reef platform

Wave transformation across the reef platform is compared for the same wave and water-level conditions ($H_{s,o}$ = 0.08 m, T_p = 1.4 s and h_{reef} = 0.04 m), but with and without a reef island present (runs #E4 and #C4, respectively; Figure 3). In the time series of the water surface elevation (Figure 3 – left panels), individual waves and wave groups can be traced across the reef platform. The offshore wave groups seaward of the reef platform become 'bulges' of water on the reef platform. A dramatic change in wave characteristics at the reef edge is apparent; the incident wave height $H_{s,INC}$ decreases and the infragravity wave height $H_{s,IG}$ increases as soon as the incident waves start to break (Figure 3 – right panels). As a result, the water motion on the reef platform becomes dominated by IG motion, with over 50% of the variance at IG frequencies. Such spatial pattern in hydrodynamics is very similar to previous laboratory experiments (e.g., *Ma et al.*, 2014, their Figure 2), as well as field experiments (e.g., *Beetham et al.*, 2016, their Figures 2 and 3). $H_{s,INC}$ across the reef is virtually identical for the runs with and without a reef island, but $H_{s,IG}$ is more than twice as large in front of a reef island (0.03–0.05 m compared to 0.015–0.02 m). Across the fore reef, where most of the waves are breaking, a small wave set-down is apparent, whereas wave set-up prevails across the reef platform (Figure 3 – lower-right panel). Wave set-up across the reef platform in the presence of an island is significantly larger (c. 0.01 m) than without an island (c. 0.005 m), most likely due to the partitioning of momentum into setup and mean flow across the platform (*Symonds et al.*, 1995). Without an island, the wave set-up is limited to the seaward part of the reef platform and decreases across the landward part of the reef platform, whereas wave set-up remains high in front of the island. This is similar to the laboratory results of *Ma et al.* (2014, their Figure 2, atoll reef) and *Yao et al.* (2012, their Figures 4–7, fringing reef), respectively, and the field results of *Jago et al.* (2007, their Figure 8).

Figure 3 here

The summary statistics of the key hydrodynamic parameters for all 18 model runs without a reef island present (test Series A–C), and averaged across the middle of the reef platform (x = 3.6 – 6.8 m; wave gauges 7 – 12), reveal a strong dependency of these parameters on the offshore wave height $H_{s,o}$ and the still water depth across the reef platform h_{reef} (Figure 4). Wave set-up increases with offshore wave height and decreasing water depth, and reaches a maximum value of 0.017 m (21% of the offshore wave height). $H_{s,INC}$ increases with both offshore wave height and water depth, and attains a maximum of 0.029 m. $H_{s,IG}$ increases with offshore wave height and decreasing water depth, and the maximum value is 0.020 m (25% of the offshore wave height). The percentage infragravity energy increases both with decreasing offshore wave height and water depth, and reaches a maximum value of 82%. As commonly found in field settings, the water motion on the reef platform is very strongly modulated by the tide, with incident wave dissipation and relative infragravity wave energy maximised at low tide levels (e.g., *Young*, 1990; *Brander et al.*, 2004; *Beetham et al.*, 2015).

Figure 4 here

Comparison between co-located time series of wave groups A_t and that of the infragravity wave motion $\eta_{t,IG}$ reveals that these two signals are strongly correlated (Figure 5, upper panels), with correlation coefficients in excess of 0.7 (Figure 5, lower panels). Seaward of the reef platform (at x = 10 m), there is a strong wave group signal and a weak IG wave signal, and $\eta_{t,IG}$ is in anti-phase with A_t (Figure 5, lower-left panel). Cross-correlation analysis further reveals that the IG signal lags 3–15 s behind the wave groups. Across the reef platform (x = 6.8 m), there is a weak wave group signal and a strong IG wave signal, and $\eta_{t,IG}$ is in-phase with A_t, with the maximum correlation at zero lag (Figure 5, lower-middle panel). The IG wave motion across the reef platform has a stronger correlation with the wave groups seaward of the reef platform, than with the wave groups on the reef platform (Figure 5, lower-right panel), suggesting breakpoint forcing of the IG wave motion. The lag associated with the maximum correlation is just over 2 s, and this corresponds roughly to the travel time of the waves from x = 10 m to x = 6.8 m computed using linear wave theory (just under 3 s). The key characteristic of the cross-correlation function between A_t and $\eta_{t,IG}$ is the abrupt switch from an anti-phase correlation seaward of the reef platform to an in-phase correlation across the reef platform, similar to that found in the laboratory by *Janssen et al.* (2003, their figure 3), and in the field by *Pomeroy et al.* (2012, their Figure 5) and *Gawehn et al.* (2016, their Figure 5).

Figure 5 here

Wave spectra of the water surface elevation and cross-correlation functions between A_t and $\eta_{t,IG}$ were computed for three different runs (#A4, #C5 and #E4) using all wave gauge data to map the spatial evolution of the IG signal across the reef platform (Figure 6). Wave forcing for all runs was with $H_{s,o}$ = 0.08 m. Run #A4 was selected as it had the strongest cross-correlations due to the low water level (h_{reef} = 0 m) and the long wave period (T_p = 2.3 s), whereas runs #C5 and #E4 were selected as they represent identical hydrodynamic conditions (h_{reef} = 0.02 m; T_p = 1.4 s), but enable comparison between absence and presence of a reef island, respectively. All runs show a rapid transition from incident-wave dominated water motion across the fore reef to infragravity-dominated water motion across the reef platform (Figure 6, upper panels). The vast majority of the IG energy is at frequencies < 0.1 Hz and there is often a broad peak around 0.05 Hz.

Figure 6 here

The cross-correlations between the co-located A_t and $\eta_{t,IG}$ (Figure 6, middle panels) appear to show the presence of a bound long wave, as there is a negative correlation between A_t and $\eta_{t,IG}$ across the fore reef, although the maximum negative correlation does not occur at zero lag. In contrast, the correlations across the reef platform show an in-phase relationship between A_t and $\eta_{t,IG}$, i.e., the largest wave groups coincide with the crests of the IG waves. The cross-correlations involving the 'offshore' A_t and $\eta_{t,IG}$ across the model domain shows shoreward-propagating IG motion across the reef platform for runs without island (#A4 and #C5), as illustrated by the increasing lag across the reef platform of the maximum positive correlation (Figure 6, lower panels). For the run with a reef island present (#E4), the incoming IG wave is observed, but there is also an outgoing IG wave resulting from reflection at the island shoreline (Figure 6, lower-right panel). For the high tide and short-period wave run without an island present (#C5), there is also a weak signal associated with an outgoing IG wave reflected and 180° phase-shifted off the back reef slope (Figure 6, lower-mid panel).

The progressive nature of the IG wave motion across the reef platform in the absence of an island and the superposition of an incoming and outgoing IG wave when an island is present is confirmed by cross-spectral analysis between time series of η_t from different locations (x = 7.4 and 5.6 m) on the platform (Figure 7). The normalised spectra show a dramatic transformation of wave energy from the incident to the infragravity frequencies across the 2-m stretch of reef platform, regardless of whether there is an island present (#C5) or not (#E4) (Figure 7, upper panels). In the absence of an island, the η_t time series at the two locations on the reef platform are coherent at the 95% confidence level across practically the whole IG domain (frequencies < 0.35 Hz), but in the presence of an island, the coherence K^2_{sig} fluctuates widely across the frequency domain, frequently dipping below the 95% confidence level (Figure 7, middle panels). The latter is diagnostic of a standing wave structure, with K^2_{sig} minima representing nodes near the wave gauge location(s). The progressive versus standing nature of the IG wave motion across the reef platform is even better illustrated by the phase spectra (Figure 7, lower panels). The phase spectrum for run #C5 (without island) shows a linear phase change with frequency, indicative of progressive wave motion, whereas the phase spectrum for run #E4 (with island), and taking into account 95% confidence levels for the phase angles of better than 20° given the high K^2_{sig} values, shows the water motion in-phase (0°) for frequencies < 0.07 Hz, in anti-phase (±180°) for up to frequencies of 0.35 Hz.

Figure 7 here

3.2 Validation of XBeach numerical model

The physical model results of Test Series B (mid-tide) were used to validate the XBeach model through comparison of the across-reef variability in wave conditions and water level (Figure 8). The numerical model was run at the prototype scale and the small-scale laboratory results were scaled up by a geometric scaling factor of 50. The prototype wave conditions for the runs used in the validation are $H_{s,o}$ = 2, 3 and 4 m, and T_p = 16.3 s (equivalent to runs #B2, #B4 and #B6). There is overall very good agreement between the physical and numerical model results of the incident wave height $H_{s,INC}$ and wave set-up profile; even the reflection of the incident waves off the reef edge leading to a reduction in $H_{s,INC}$ between x = 500 and 600 m (due to the nodal structure) is reproduced (Figure 8, upper panels). The infragravity wave height $H_{s,IG}$ is well-predicted for the least energetic wave condition (#B2; H_s = 2 m), but over-predicts $H_{s,IG}$ for the fore reef and the first part of the reef platform, and under-predicts $H_{s,IG}$ for the second part of the reef platform for the more energetic runs (#B4 and #B6; H_s = 3 and 4 m) (Figure 8, middle panels). For the most energetic wave condition, the difference between measured and predicted $H_{s,IG}$ is always less than 25%. The modelled wave set-up profile also fits the measurements quite well for the less energetic wave conditions (#B2 and #B4), but significantly under-predicts the set-down across the fore reef (by c. 50%) and over-predicts the wave set-up across the seaward part of the reef platform (by c. 30%) for the most energetic wave conditions (#B6) (Figure 8, lower panels).

Figure 8 here

The numerical model results were also used to validate the cross-correlation between the wave group signal A_t and the IG wave motion $\eta_{t,IG}$ for the up-scaled physical model forcing conditions of runs #A4, #C5 and #E4. The model results are presented in Figure 9 and are directly comparable to the physical model results shown in Figure 6. Note that the numerical model domain extends significantly further seaward than the physical model domain; the solid circle in the lower panels of Figure 9 represents the prototype-equivalent position of the seaward-most wave gauge in the physical model experiment. The physical and numerical model results are remarkably consistent and highlight the following salient features: (1) rapid transition from incident to infragravity wave energy at the fore reef and the domination of IG energy across the reef platform (Figure 9, upper panels); (2) a weak incoming IG wave seaward of the reef platform (BLW: negative correlation between A_t and $\eta_{t,IG}$) (Figure 9, middle panels); (3) a strong outgoing IG wave (BFLW: negative correlation between A_t and $\eta_{t,IG}$) and incoming IG wave (BFLW: positive correlation between A_t and $\eta_{t,IG}$), both originating at the reef edge (9, lower panels); (4) an outgoing IG wave originating at the reef island (reflection of the incoming BFLW: positive correlation between A_t and $\eta_{t,IG}$) (Figure 9, lower-right panel); and (5) an outgoing IG originating at the back of the reef (reflection of the incoming BFLW off the back reef slope with 180^o phase-shifting (negative correlation between A_t and $\eta_{t,IG}$ (Figure 9, lower-mid panel).

Figure 9 here

The main discrepancies between the wave statistics derived from the laboratory measurements and the numerical model results are attributed to the very challenging hydrodynamic conditions that arise in the breaker zone due to the extremely steep slope of the fore reef (1:2.3). Calibrating the model, e.g., through modifying the parameters in the roller model or the drag coefficient, may result in improved model performance. The two key differences in the A_t – $\eta_{t,IG}$ cross-correlations between the physical and numerical model are the generally stronger correlations in the numerical model results (as expected, since the numerical model is a simplified representation of reality) and the absence of a clear outgoing BFLW seaward of the fore reef in the physical model results (because the seaward-most wave probe is located too close to the reef platform to be able to detect the outgoing BFLW). The numerical model performance is considered sufficiently good for the model to be used to investigate in more detail the IG wave generation mechanisms and extend the parameter space beyond conditions that were experienced in the laboratory experiment.

3.3 Numerical experiments

The physical model results were obtained for a fore reef slope of 1:2.3 and water depths over the reef platform h_{reef} of 0, 0.02 and 0.04 m (proto-type h_{reef} = 0,1 and 2 m). XBeach was used to explore the influence of the fore reef slope and h_{reef} on the IG wave characteristics and generation mechanism by conducting a large number of model simulations with constant wave conditions ($H_{s,o}$ = 2.5 m and T_p = 12.5 s), but varying fore reef slope and h_{reef} (refer to Section 2.2). The cross-correlation function between the lowpass-filtered wave envelope A_t at the seaward model boundary (x = 1000 m) and the infragravity wave signal $\eta_{t,IG}$ at each of the model grid points for a subset of this modelled data is shown in Figure 10.

Figure 10 here

The key feature of Figure 10 is the fundamental difference in the A_t – $\eta_{t,IG}$ cross-correlation 'signature' between the steepest (1:1) and gentlest (1:20) slope. For the steepest slope, and irrespective of h_{reef}, the cross-correlation switches practically instantly from negative to positive at the seaward edge of reef platform (blue-to-red at reef edge in Figure 10, left panels). Whether this reflects a transition from BLW into BFLW or represents the BFLW overpowering the BLW is unclear. In addition, a strong outgoing BFLW also originates at the reef edge. For the gentlest slope and large water depth across the reef platform (h_{reef} ≥ 4 m), the BLW continues to propagate across the reef platform, whilst at the same time developing a leading crest (blue-next-to-red across the reef platform in Figure 10, upper-right panels). A similar signature was reported by *Pomeroy et al.* (2012; their Figure 10), which they, following *Baldock* (2006, his Figure 5), interpret as the development of an elevated surface elevation in front of the wave group as a result of 'dynamic setup'. For the gentlest slope and MSL below the reef platform (h_{reef} < 0 m), the dynamic set-up appears to develop earlier and across the fore reef (Figure 10, lower-right panels). The cross-correlation signature for the intermediate slope (1:10) has elements of both the BLW and the BFLW (Figure 10, middle panels). It is also worth noting that a significant outgoing BFLW is present in all cross-correlations shown in Figure 10.

The cross-correlations are useful in that the different IG wave forcing mechanism can be identified, but the strength of the cross-correlations is not necessarily related to the energy and therefore importance of the IG wave motion. To address the actual IG wave energy, as well as help identify the importance of the BLW versus BFLW mechanisms, the IG wave signal was partitioned into an incoming and outgoing IG wave using *Guza et al.* (1984; Eqs 6 and 7), and the transformation of the incoming, outgoing and total IG wave signal across the model domain is plotted in Figure **11**. The wave transformation pattern for the total IG wave motion is somewhat confusing due to its cross-cross pattern (Figure **11**, second row of panels), but once the IG signal is divided into its two components (Figure **11**, third and fourth row of panels), a clear picture emerges that confirms the interpretations of the cross-correlation plots: both the BLW and BFLW mechanism are valid, but which mechanism is dominant depends on the fore reef slope, with the steeper slope favouring the BFLW and the gentler slope the BLW mechanism. What Figure **11** adds to this discussion is that the IG energy across the reef platform, as well as the outgoing energy seaward of the platform, is largest for the steepest fore reef. The average significant IG wave height across the reef platform (based on $H_s = 4\sigma$, where σ is the standard deviation associated with $\eta_{t,IG}$, for lowpass filter of $1/4T_p$) for fore reef slopes of 1:1, 1:10 and 1:20 is 0.41, 0.30 and 0.29 m, respectively. Similarly, the average maximum orbital velocity of the IG wave motion across the reef platform (based on $U_m = 2\sigma$, where σ is the standard deviation associated with $u_{t,IG}$, for lowpass filter of $1/4T_p$) for the same fore reef slopes is 0.50, 0.34 and 0.33 m s^{-1}, respectively. It seems, therefore, that the role of IG waves to impact coastal flooding, as well as contribute to sediment transport processes, increases with increasing fore reef slope.

*Figure **11** here*

XBeach was further used to model the incident and infragravity wave characteristics across reef platforms for varying fore reef slopes, wave conditions and water levels. As outlined in Section 2.2, a very large number (c. 4000) model runs were carried out with the boundary conditions selected randomly from a wide parameter space ($H_{s,o}$ = 1–6 m, T_p = 4–20 s, h_{reef} = -3 to +3 m, wave steepness 0.003–0.05, fore reef gradient = 1:1–1:50) to determine which factors are most important in controlling the infragravity wave height across the reef platform. The runs were all set up with a 200-m wide reef platform and for 21 points across the reef platform (every 10 m), the water level time series was used to obtain the significant infragravity wave height by integrating the variance σ^2 over the wave spectrum from $0.05/T_p$ to $0.5/T_p$, and $H_{s,IG} = 4\sigma$. These 21 estimates of $H_{s,IG}$ were subsequently averaged across the 200-m wide reef platform to obtain the reef-averaged IG wave height $<H_{s,IG}>$.

To combine the model results for the widely varying forcing conditions, both $<H_{s,IG}>$ and h_{reef} are normalised by the offshore significant wave height $H_{s,o}$. The data are then plotted as a function of fore reef slope and $h_{reef}/H_{s,o}$ in Figure **12**, with the size and colour of the symbols proportional to $<H_{s,IG}>/H_{s,o}$. The results show that there appears to be a 'sweet spot', characterised by a fore reef slope > 1/6 and $h_{reef}/H_{s,o}$ between -0.25 and +0.75, where $<H_{s,IG}>/H_{s,o}$ is maximised with values of 0.2–0.3 (rectangle in Figure **12**, upper panel). The mechanism for IG generation for such conditions is the BFLW and the significantly smaller values for $<H_{s,IG}>/H_{s,o}$ for the gentler fore reef gradients are attributed to the BLW mechanism. For $h_{reef}/H_{s,o} < -0.25$, the reef platform is only affected by swash action, whereas for $h_{reef}/H_{s,o} > 0.75$ a significant part of the incident waves are breaking/shoaling on the horizontal shore platform, inhibiting BFLW generation. There is also a significant effect of T_p on the results: within the 'sweet spot' region, $<H_{s,IG}>/H_{s,o}$ values for long-period waves are 20–40% larger than for short-period waves (Figure **12**, lower panels).

*Figure **12** here*

4. Discussion

Combining the results of a small-scale laboratory experiment and numerical modelling using a phase-resolving (i.e., non-hydrostatic) wave model (XBeach), new insights are obtained into the dynamics of infragravity waves across (coral) reef platforms. The key factor that controls the mechanism of IG wave generation is the slope of the fore reef. For slopes in excess of 1:10, the cross-correlation signature between wave groups and IG wave motion clearly demonstrates the generation of an incoming and outgoing BFLW, as predicted by *Symonds et al.* (1982). For smaller fore reef slopes, the release of the BLW (*Longuett-Higgins and Stewart*, 1963) is more dominant, as demonstrated by a shoreward propagating set-down wave across the reef platform. Distinguishing between the two mechanisms is made difficult by the development of the dynamic set-up across the fore reef slope (*Baldock*, 2006), but a clear difference between the BFLW and BLW mechanism is the generation of an energetic outgoing IG wave in the former case.

Previous research (*Baldock*, 2012; *Contardo and Symonds*, 2013) suggests that a value of the $\xi_{surfbeat}$ parameter (Eqs. 1 and 2) of 0.05–0.1 separates the two IG wave regimes. Inserting Eq. (2) into Eq. (1) yields:

$$\xi_{surfbeat} = \left(1/\sqrt{2\pi}\right)\left(T_{IG}/T_p\right)\sqrt{\gamma}h_x \qquad \textbf{(Eq. 8)}$$

where T_{IG} and T_p are the infragravity and incident wave period, respectively, and γ is the breaker criterion H_b/h_b. Assuming a typical IG-wave period T_{IG} of 4 times the incident-wave period T_p and an irregular breaker criterion of H_b/h_b = 0.5, Eq. 8 reduces to $\xi_{surfbeat} \approx 1.13h_x$, and $\xi_{surfbeat}$ is independent of the incident wave height or period. The XBeach model results suggest that the BFLW mechanisms dominates when the fore reef slope $h_x > 0.1$. Inserting this value into the simplified equation for $\xi_{surfbeat}$ results in a value of 0.11, which is close to the upper bound suggested by *Baldock* (2012) and *Contardo and Symonds* (2013) for separating the BLW from the BFLW mechanism. A BFLW mechanism for IG wave generation in coral reef environments, with their characteristic steep fore reef slopes, has also been argued for by *Péquignet et al.* (2009) and *Pomeroy et al.* (2012). In the latter study, the dominance of breakpoint forcing in generating IG waves across reef platforms was concluded based on comparing XBeach model runs with and without the BLW and BFLW mechanism. However, the XBeach-modelled cross-correlation between the incident short-wave envelope A_t and the IG wave time series at all locations $\eta_{t,IG}$ presented by *Pomeroy et al.* (2012; their Figure 10), and based on their field conditions with a fore reef slope of 1/20, shows evidence of both the BLW and BFLW mechanism of IG wave generation. The BFLW mechanism is more effective in generating IG energy than the release of the BLW and this is demonstrated by the larger amounts of infragravity energy across reef platforms with steeper fore reefs compared to those with gentle slopes (Figure **12**). This dependency of IG wave height on fore reef slope has also been demonstrated by *Quataert et al.* (2015; their Figure 4). Both our results and those of *Quataert et al.* (2015) suggest that the largest (relative) infragravity wave heights occur for fore reef slopes ranging from 1/2 to 1/5. The agreement is not surprising as the same numerical model was used, but the significance is that most natural fore reef slopes tend to be ranging from 1/10 to 1/20 (cf. *Quataert et al.*, 2015; their Table 1); therefore, the importance of the BLW mechanism of IG generation should not be excluded for natural coral reef settings.

In the previous sections, IG wave heights on the reef platform have been computed using a 1D model, with a smooth bed and no presence of an island on the reef flat. While this modelling approach closely resembles the set-up of the physical model experiment described in Section 2.1, a 1D approach necessarily assumes alongshore-uniform hydrodynamics, which in the case of the XBeach model implies infinitely long-crested waves. This assumption may be expected to influence the IG wave energy presented in Section 3, as directional wave spreading is known to affect infragravity wave dynamics on open coasts (e.g., *Guza and Feddersen*, 2012). Furthermore, although the physical model experiments were carried out with a smooth plywood bottom, natural coral reefs may be substantially rougher, leading to greater wave energy loss across the reef platform. Finally, analysis of the physical model experiments has shown that the presence of an island on the reef flat substantially affects infragravity wave heights on the reef flat.

To address these issues, 107 combinations of wave height, period, water level and fore reef slope that span the range of conditions simulated by the 1D XBeach model (termed 'reference' simulations; Section 2.2) were selected. These conditions were subsequently re-simulated in three separate sensitivity analyses (termed 'sensitivity' simulations) to, respectively, investigate the effect of 2D modelling to include directional wave spreading, the presence of an island, and the importance of increased bed roughness, on the main conclusions found in Section 3.

In the directional wave spreading sensitivity analysis, the sensitivity simulations were run using the non-hydrostatic XBeach model in 2DH (depth-averaged, cross-shore and alongshore) mode. The model bathymetry was kept alongshore uniform and identical to the equivalent simulations in the 1D models, but the effect of directional wave spreading is inherently included within the model domain. The directional spreading sensitivity models were set up with an alongshore width to include at least three offshore wave lengths and an alongshore grid resolution equal to that of the cross-shore resolution at the offshore boundary. Cyclic boundary conditions were imposed on the lateral boundaries of the model to remove lateral boundary wave-shadowing effects. The directional wave spreading sensitivity simulations were forced using the same water levels and wave spectral conditions as in the equivalent 1D simulations, where the directional wave spreading at the model boundary was 24° and the main wave angle was perpendicular to the reef. Note that, although the 1D simulations do not account for directional wave spreading within the model domain, both the 1D and 2DH models account for directional spreading in the computation of the BLW imposed on the model boundary. Both the 1D and 2DH simulations are therefore forced by the same incident BLW conditions. All other model parameters in the sensitivity simulations were kept identical to the reference simulations.

In the island and bed roughness sensitivity analyses, the sensitivity simulations were run using a 1D XBeach model. In the case of the island sensitivity simulations, the model bathymetry was modified to include a 1:8 beach slope at the end of the 200 m coral reef platform, where the height of the beach was set such that no wave overtopping over the beach took place. In the bed roughness sensitivity simulations, the reef profile of the reference simulations was used, but the bed friction was increased to a uniform value $c_f = 0.1$ (cf. *Pearson et al.*, 2017).

Figure **13** shows the absolute (top panels) and relative (bottom panels) difference in simulated IG wave height between the reference simulations ('Ref' in the figure) and sensitivity simulations ('Sen' in the figure), where the relative difference $\Delta H_{rel,Sen\text{-}Ref}$ is defined as:

$$\Delta \mathrm{H}_{rel,Sen-Ref} = \frac{\langle H_{IG,Sen}/H_{s,o,Sen}\rangle - \langle H_{IG,Ref}/H_{s,o,Ref}\rangle}{\langle H_{IG,Ref}/H_{s,o,Ref}\rangle} \qquad \textbf{(Eq. 9)}$$

where the angle brackets indicate averaging over all output points and the subscripts $_{Sen}$ and $_{Ref}$ refer to the sensitivity and equivalent reference simulations, respectively.

Figure **13** (left panels) demonstrates that the relative difference in IG wave height in the directional wave spreading sensitivity simulations is relatively modest, but that in general lower infragravity wave heights occur in the 2DH simulations than in the 1D simulations (mean $\Delta H_{rel,Sen\text{-}Ref}$ of -14% and -2% for wave periods less than 12 s and greater than 12 s, respectively), which may be expected considering the absence of directional wave spreading within the domain of the 1D simulations. The figure furthermore shows that the largest relative difference between the 1D and 2DH simulations occurs for $h_{reef}/H_{s,o}$ of about -1.1, where IG waves on the reef platform in the 1D simulations are substantially larger (>60%) than those in the 2DH simulations. This difference may be a result of the fact that IG waves are unable to spread laterally in the 1D simulations, and are therefore forced to go over the reef crest. Interestingly, the 2DH simulations appear to show slightly (0–19%) larger IG wave heights for $h_{reef}/H_{s,o}$ values between 0 and 1 than the 1D simulations. This relative water depth corresponds somewhat to the 'sweet spot' found in Section 3.3, indicating that alongshore variations in water level due to directional wave spreading may be increasing the BFLW generation mechanism at these water depths. Encouragingly, the difference between the 1D and 2DH simulations remains relatively small for shallow fore reef slopes (1/50–1/25), where the lack of wave spreading may conceivably affect energy transfer to the infragravity wave in the 1D simulations via the BLW generation mechanism, indicating that this model limitation in the 1D simulations is unlikely to greatly affect the results found in Section 3.

*Figure **13** here*

The results of the island sensitivity simulations in Figure **13** (centre panels) show that the presence of an island on the reef substantially increases the contribution of IG waves to the total wave spectrum on the reef platform. For conditions in which IG waves are greater than 10% of the offshore wave height (i.e., $h_{reef}/H_{s,o} > -0.5$), the presence of an island leads to approximately 50% (for wave periods less than 12 s) to 100% (for wave periods greater than 12 s) greater IG wave heights on the reef platform, which is qualitatively in line with the findings of the physical model experiment in Section 3.1. Interestingly, $\Delta H_{rel,Sen\text{-}Ref}$ is relatively insensitive to changes in $h_{reef}/H_{s,o}$ within this range. While the modelled increase in IG wave height, and difference in increase between short and long-period incident-band waves, may in general be representative for natural coral reef island systems, it is important to note that both are likely to be sensitive to the length of the reef platform fronting the island, and hence potential for standing waves to occur.

Finally, the results of the bed roughness sensitivity simulations are presented in Figure **13** (right panels). The figure shows that high values of bed roughness ($c_f = 0.1$) greatly reduce (14–97%) IG wave height on the coral reef platform. This reduction is slightly greater in simulations with shorter-period incident-band waves (periods less than 12 s) than in simulations with longer-period incident-band waves. Importantly, however, the results show that the effectiveness of bed roughness in damping the IG wave height on the reef platform is dependent on the water depth, with generally decreasing damping with increasing relative water depths over the platform up to $h_{reef}/H_{s,o}$ values of 0.25–0.5, followed by constant, or even increasing damping for $h_{reef}/H_{s,o}$ values greater than 0.5. These result mean that although IG waves on rough reef platforms may be expected to be smaller than those presented in Section 3.3, less damping of the IG waves will occur at $h_{reef}/H_{s,o}$ values of 0.5, than for lower (and partly also for greater) relative water depths. This change in damping effect for varying relative water depth maintains the 'sweet spot' for IG wave generation found in Section 3.3.

Once the IG waves are generated and/or released near the seaward edge of the reef platform, they will be subjected to bed friction and are likely to decrease in absolute importance as they propagate shoreward, especially for wide and rough reef platforms (e.g., *Pearson et al.*, 2017). Nevertheless, despite the shoreward-propagating IG waves experiencing substantial frictional dissipation that limit the amount of IG energy reaching the shoreline, the rate of IG wave decay is considerably smaller than for the short waves (*Pomeroy et al., 2012*) and the presence of IG wave motion has significant implications for geomorphic processes on coral reef platforms and island dynamics. First, long wave motions propagating across reef surfaces provide important controls on current and circulation processes across platforms. Second, velocities associated with these wave types are sufficient to entrain and transport detrital sand-size materials on reef surfaces and govern vectors of sediment transport (e.g., *Pomeroy et al.*, 2015). Third, results also confirm the importance of long period wave motions as primary processes on reef surfaces that control island inundation at contemporary sea levels (e.g., *Beetham et al.*, 2016; *Cheriton et al.*, 2016). Notably, results indicate that fore reef slope influences wave propagation behaviour and consequently, susceptibility to island overtopping by long period wave motions. All these geomorphic implications are expected to be most significant for coral reef platforms with the steepest fore reefs and the narrowest and smoothest platforms, and under energetic wave conditions.

Conclusions

A small-scale (1:50) laboratory experiment, complimented by proto-type numerical XBeach modelling, was conducted to investigate the characteristics of infragravity (IG) wave motion on coral reefs and quantify the important factors controlling IG wave height across the platform.

Despite the small-scale of the laboratory experiment, the results confirm across-platform wave transform trends previously demonstrated in field studies (e.g., incident wave dissipation, IG wave generation, wave set-up across the reef platform). The small-scale laboratory results were also successfully validated using the phase-resolving (i.e., non-hydrostatic) XBeach model run at the proto-type scale, allowing further numerical exploration beyond the laboratory simulations. The 1D numerical model results were replicated using a 2DH model, forced with the same boundary conditions. The 2DH model generally predicts lower IG wave heights, but the relative difference in IG wave height is modest, especially when the reef platform is submerged, confirming the wider applicability of the 1D numerical model results to real world coral reef environments.

Using cross-correlation analysis between the incident short-wave envelope A_t and the IG wave time series at all locations $\eta_{t,IG}$, the slope of the fore reef is identified as the key factor controlling the mechanism of infragravity wave generation. For steep slopes (> 1/10), IG wave motion is dominated by landward and seaward propagating breakpoint-forced long waves (BFLWs) and there is no evidence of the bound long wave (BLW) propagating onto the reef platform. For more gentle slopes (1/20), evidence for the BFLW mechanism remains, but BLWs can also be observed travelling from the fore reef onto the reef platform. For increasingly gentle slopes, it is inferred that BLWs become the dominant mechanism for IG wave generation.

The BFLW mechanism is a more effective generator of IG energy that the BLW mechanism, and the most energetic IG motion (normalised by incident wave motion) is generated on reef platforms with a fore reef slope > 1/6. The still water level relative to the reef platform h_{reef} is also a key factor and the most energetic IG wave motion is generated for a ratio between h_{reef} and offshore incident wave height $H_{s,o}$ between -0.25 and 0.75, i.e., when most waves break across the reef slope and a fully saturated surf zone extends across the reef platform. The presence of an island on the reef platform substantially increases the contribution of IG waves to the total wave spectrum on the reef platform, but increased reef surface roughness reduces IG importance. Under the most optimal conditions, the IG wave height averaged across the reef platform is 20–30% of the incident offshore wave height, and the geomorphic influence of IG waves is most significant for coral reef platforms with energetic waves breaking on the steepest fore reefs.

Acknowledgements

We would like to thank the COAST lab staff and MSc students Amy Gosnell and Josef Saunders for their help with the wave flume experiment. The physical model data discussed in this paper were collected by MT and the physical laboratory experiment was funded through Catalyst Seeding funding provided by the New Zealand Ministry of Business, Innovation and Employment and administered by Royal Society of New Zealand, and grant awarded to MF and PK. The numerical modelling was carried out by GM, RMC and AVD. All data analysis was conducted by GM and all authors contributed to the writing of this paper. RMC and AVD were funded through Deltares' Strategic Research

Program ‘Hydro- and morphodynamics during extreme events’. The physical laboratory data are available from https://doi.org/10.24382/mwaw-5864.

References

Bakker, A. T. M., M. F. S. Tissier, and B. G. Ruessink (2014), Shoreline dissipation of infragravity waves, *Cont. Shelf Res., 72,* 73–82, doi:10.1016/j.csr.2013.11.013.

Battjes, J. A., H. J. Bakkenes, T. T. Janssen, and A. R. van Dongeren (2004), Shoaling of subharmonic gravity waves, *J. Geophys. Res. 109*, C02009, doi:10.1029/2003JC001863.

Baldock, T. E. (2006), Long wave generation by the shoaling and breaking of transient wave groups on a beach, *Proc. R. Soc. A, 462(2070)*, 1853–1876.

Baldock, T. E. (2012), Dissipation of incident forced long waves in the surf zone—Implications for the concept of “bound” wave release at short wave breaking, *Coastal Eng., 60,* 276–285, doi:10.1016/ j.coastaleng.2011.11.002.

Beauchamp, K. G. and C. K. Yuen (1979), *Digital Methods for Signal Analysis*, Allen & Unwin, London, 316 pp.

Becker, J. M., M. A. Merrifield, and M. Ford (2014), Water level effects on breaking wave setup for Pacific Island fringing reefs, *J. Geophys. Res. Oceans, 119*, 914–932, doi:10.1002/2013JC009373.

Beetham, E., P. S. Kench, J. O’Callaghan, and S. Popinet (2015), Wave transformation and shoreline water level on Funafuti Atoll, Tuvalu, *J. Geophys. Res. Oceans, 121*, 311–326, doi:10.1002/2015JC011246.

Beetham, E., P. S. Kench, and S. Popinet, (2017) Future reef growth can mitigate physical impacts of sea-level rise on atoll islands. *Earth’s Future, 5*, doi:10.1002/2017EF000589.

Bosserelle, C., Lal, D., Movono, M., Begg, Z., Kumar, S., Reddy, S., Beetham, E., Pohler, S., Kench, P. and Krüger, J., 2016. *Waves and Coasts in the Pacific (WACOP)*, Fatato (Tuvalu), Oceanographic, Topographic data Collection, Pacific Community, SPC technical Report SPC00045.

Brander, R. W., P. S. Kench, and D. Hart (2004), Spatial and temporal variations in wave characteristics across a reef platform, Warraber Island, Torres Strait, Australia, *Mar. Geol., 207*, 169–184, doi:10.1016/j.margeo.2004.03.014.

Cheriton, O. M., C. D. Storlazzi, and K. J. Rosenberger (2016), Observations of wave transformation over a fringing coral reef and the importance of low-frequency waves and offshore water levels to runup, overwash, and coastal flooding, *J. Geophys. Res. Oceans, 121,* 3121–3140, doi:10.1002/2015JC011231.

Contardo, S., and G. Symonds (2013), Infragravity response to variable wave forcing in the nearshore, *J. Geophys. Res., 118*, 7095–7106, doi:10.1002/2013JC009430.

Ferrario, F., M. W. Beck, C. D. Storlazzi, F. Micheli, C. C. Shepard, and L. Airoldi (2014), The effectiveness of coral reefs for coastal hazard risk reduction and adaptation, *Nat. Commun., 5*, 1–9, doi:10.1038/ncomms4794.

Ford, M. R., J. M. Becker, and M. A. Merrifield (2013), Reef flat wave processes and excavation pits: Observations and implications for Majuro Atoll, Marshall Islands, *J. Coastal Res., 29(3)*, 545–554, doi:10.2112/jcoastres-d-12-00097.1.

Gawehn, M., A. van Dongeren, A. van Rooijen, C. D. Storlazzi, O. M. Cheriton, and A. Reniers (2016), Identification and classification of very low frequency waves on a coral reef flat, *J. Geophys. Res. Oceans, 121*, doi:10.1002/2016JC011834

Gourlay, M. R. (1996a), Wave set-up on coral reefs. 1. Set-up and wave-generated flow on an idealised two dimensional horizontal reef, *Coast. Eng., 27*, 161–193, doi:10.1016/0378-3839(96)00008-7.

Gourlay, M. R. (1996b), Wave set-up on coral reefs. 1. Set-up on reefs with various profiles, *Coast. Eng., 28*, 17–55, doi:10.1016/0378-3839(96)00009-9.

Grady, A. E., L. J. Moore, C. D. Storlazzi, E. Elias, and M. A. Reidenbach (2013), The influence of sea level rise and changes in fringing reef morphology on gradients in alongshore sediment transport, *Geophys. Res. Lett., 40,* 3096–3101, doi:10.1002/grl.50577.

Guza, R.T., and E. B. Thornton (1985), Observations of surf beat, *J. Geophys. Res., 90*, 3161–3172, doi:10.1029/JC090iC02p03161.

Guza, R. T., and F. Feddersen, (2012), Effect of wave frequency and directional spread on shoreline runup. *Geophys. Res. Lett.,* 39 (L11607), doi:10.1029/2012GL051959.

Hardy, T. A., and I. R. Young (1996), Field study of wave attenuation on an offshore coral reef, *J. Geophys. Res., 101(C6), 14*, 311–14, doi:10.1029/96JC00202.

Harris, D., A. Vila-Concejo, J. Webster, and H. Power (2015). Spatial variations in wave transformation and sediment entrainment on a coral reef sand apron. *Mar. Geol., 363*, 220–229, doi:10.1016/j.margeo.2015.02.010.

Henderson, S. M., and A. J. Bowen (2002), Observations of surf beat forcing and dissipation, *J. Geophys. Res., 107(C11), 3193*, doi:10.1029/ 2000JC000498.

Henderson, S. M., R. T. Guza, S. Elgar, T. H. C. Herbers, and A. J. Bowen (2006), Nonlinear generation and loss of infragravity wave energy, *J. Geophys. Res., 111, C12007*, doi:10.1029/2006JC003539.

Hoeke, R. K., C. D. Storlazzi, and P. V. Ridd (2013a), Drivers of circulation in a fringing coral reef embayment: A wave-flow coupled numerical modeling study of Hanalei Bay, Hawaii, *Cont. Shelf Res., 58*, 79–95, doi:10.1016/j.csr.2013.03.007.

Inch, K., M. Davidson, G. Masselink, G., and P. Russell (2017), Observations of nearshore infragravity wave dynamics under high energy swell and wind-wave conditions, *Cont. Shelf Research*, *138*, 19–31, doi:10.1026/j.csr.2017.02.010.

Jago, O. K., P. S. Kench, and R. W. Brander (2007), Field observations of wave-driven water-level gradients across a coral reef flat, *J. Geophys. Res., 112, C06027*, doi:10.1029/2006JC003740.

Janssen, T. T., J. A. Battjes, and A. R. van Dongeren (2003), Long waves induced by short wave groups over a sloping bottom, *J. Geophys. Res., 108(C8), 3252*, doi:10.1029/2002JC001515.

Jenkins G. M., and D. G. Watts (1968), *Spectral Analysis and its Applications*, Holden-Day, San Francisco, 525 pp.

Kench P.S. (1998), Physical controls on development of lagoon sand deposits and lagoon infilling in an Indian Ocean atoll, *J. Coastal Res., 14*, 1014–1024.

Kench, P.S. (2013), Coral Systems, In: John F. Shroder (Editor-in-chief), Sherman, D.J. (Volume Editor). *Treatise on Geomorphology*, Vol 10, Coastal Geomorphology, San Diego: Academic Press, 328–359.

Kench, P.S., and Brander, R.W. (2006), Wave processes on coral reef flats: Implications for reef geomorphology using Australian case studies. *J. Coast. Res., 22*, 209–223.

Kench P.S., and R.F. McLean (2004), Hydrodynamics and sediment flux of hoa in an Indian Ocean atoll, *ESPL, 29*, 933–953, doi:10.1002/esp.1072.

Kench, P.S., E. Beetham, C. Bosserelle, J. Kruger, S. Pohler, G. Coco, and E. Ryan (2017), Nearshore hydrodynamics, beachface cobble transport and morphodynamics on a Pacific atoll motu, *Mar. Geol, 389*, 17–31, doi:10.1016/j.margeo.2017.04.012.

List, J. H. (1986), Wave groupiness as a source of nearshore long waves. *Proc. 20th ICCE*, 497–511.

List, J. H. (1991), Wave groupiness variations in the nearshore, *Coast. Eng., 15*, 475–96, doi:10.1016/0378-3839(91)90024-B.

List, J. H. (1992), A model for the generation of two-dimensional surf beat, *J. Geophys. Res., 97(C4)*, 5623–5635, doi:10.1029/91JC03147.

Longuet-Higgins, M. S., and R. W. Stewart (1962), Radiation stress and mass transport in gravity waves with applications to 'surf beats', *J. Fluid Mech., 13*, 481–504, doi:10.1017/S0022112062000877.

Lowe, R. J., J. L. Falter, M. D. Bandet, G. Pawlak, M. J. Atkinson, S. G. Monismith, and J. R. Koseff (2005), Spectral wave dissipation over a barrier reef, *J. Geophys. Res., 110*, C04001, doi:10.1029/2004JC002711.

Lugo-Fernandez, A., H. H. Roberts, W. J. Wiseman Jr., and B. L. Carter (1998), Water level and currents of tidal and infragravity periods at Tague Reef, St. Croix (USVI), *Coral Reefs, 17*, 343–349, doi:10.1007/s003380050137.

Ma, G., S.-F. Su, S. Liu, and J.-C. Chu (2014), Numerical simulation of infragravity waves in fringing reefs using a shock-capturing non-hydrostatic model, *Ocean Eng., 85*, 54–64, doi:10.1016/j.oceaneng.2014.04.030.

Masselink, G. (1995), Group bound long waves as a source of infragravity energy in the surf zone, *Cont. Shelf Res., 15(13)*, 1525–1547, doi:10.1016/0278-4343(95)00037-2.

Masselink, G., R. T. McCall, T. G. Poate, and P. van Geer (2014), Modelling storm response on gravel beaches using XBeach-G, *Proc. ICE – Mar. Eng., 167*, 173–191, doi:10.1680/maen.14.00020.

McLean, R.F. (2011), Atoll Islands (Motu), In: Hopley, D. (Ed.), *Encyclopedia of Modern Coral Reefs: Structure, Form and Process*, Springer, Dordrecht, The Netherlands, 47–50.

Nwogu, O., and Z. Demirbilek (2010), Infragravity wave motions and runup over shallow fringing reefs, *J. Waterw. Port Coastal Ocean Eng., 136*,295–305, doi:10.1061/(ASCE)WW.1943-5460.0000050.

Ogston, A. S., C. D. Storlazzi, M. E. Field, and M. K. Presto (2004), Sediment resuspension and transport patterns on a fringing reef flat, Molokai, Hawaii. *Coral Reefs*, 23, 559–569, doi:1 0.1007/s00338-004-0415-9.

Pearson, S. G., Storlazzi, C. D., van Dongeren, A. R., Tissier, M. F. S., and Reniers, A. J. H. M. (2017), A Bayesian-based system to assess wave-driven flooding hazards on coral reef-lined coasts, *J. Geophys. Res. Oceans*, 122, doi:10.1002/2017JC013204.

Péquignet, A. C. N., J. M. Becker, M. A. Merrifield, and J. Aucan (2009), Forcing of resonant modes on a fringing reef during tropical storm Man-Yi, *Geophys. Res. Lett., 36, L03607*, doi:10.1029/2008GL036259.

Péquignet, A. C. N., J. M. Becker, M. A. Merrifield, and S. J. Boc (2011), The dissipation of wind wave energy across a fringing reef at Ipan, Guam, *Coral Reefs, 30, suppl. 1*, 71–82, doi:10.1007/s00338-011-0719-5.

Péquignet, A. C. N., J. M. Becker, and M. A. Merrifield (2014), Energy transfer between wind waves and low-frequency oscillations on a fringing reef, Ipan, Guam, *J. Geophys. Res. Oceans, 119*, 6709–6724.

Pomeroy, A., R. J. Lowe, G. Symonds, A. R. Van Dongeren, and C. Moore (2012), The dynamics of infragravity wave transformation over a fringing reef, *J. Geophys. Res., 117*, C11022, doi:10.1029/2012JC008310.

Pomeroy, A. W. M., R. J. Lowe, A. R. van Dongeren, M. Ghisalberti, W. Bodde, and D. Roelvink (2015), Spectral wave-driven sediment transport across a fringing reef, *Coastal Eng., 98*, 78–94, doi:10.1016/j.coastaleng.2015.01.005.
Quataert, E., C. Storlazzi, A. van Rooijen, O. Cheriton, and A. van Dongeren (2015), The influence of coral reefs and climate change on wave-driven flooding of tropical coastlines, *Geophys. Res. Lett., 42*, 6407–6415, doi:10.1002/2015GL064861.
Roelvink, D., A. Reniers, A. van Dongeren, J. van Thiel de Vries, R. McCall, and J. Lescinski (2009), Modelling storm impacts on beaches, dunes and barrier islands, *Coast. Eng., 56*, 1133–1152, doi:10.1016/j.coastaleng.2009.08.006.
Roeber, V., and J. D. Bricker (2015), Destructive tsunami- wave generated by surf beat over a coral reef during Typhoon Haiyan, *Nat. Commun., 6, 7854*, doi:10.1038/ncomms8854
Sheppard, C., D. J. Dixon, M. Gourlay, A. Sheppard, and R. Payet (2005), Coral mortality increases wave energy reaching shores protected by reef flats: examples from the Seychelle, *Estuar. Coast. Shelf Sci., 64,* 223–234, doi:10.1016/j.ecss.2005.02.016.
Shimozono, T., Y. Tajima, A. B. Kennedy, H. Nobuoka, J. Sasaki, and S. Sato (2015), Combined infragravity wave and sea-swell runup over fringing reefs by super typhoon Haiyan, *J. Geophys. Res. Oceans*, 120, 4463–4486, doi:10.1002/2015JC010760.
Smithers S.G. (2011), Coral cay classification and evolution, In: Hopley, D. (Ed.), *Encyclopedia of Modern Coral Reefs: Structure, Form and Process*. Springer, Dordrecht, The Netherlands, 237–253.
Storlazzi, C. D., E. Elias, M. E. Field, and M. K. Presto (2011), Numerical modeling of the impact of sea-level rise on fringing coral reef hydrodynamics and sediment transport, *Coral Reefs, 30(1)*, 23–38, doi:10.1007/s00338-010-0705-3.
Storlazzi, C. D., E. P. L. Elias, and P. Berkowitz (2015), Many atolls may be uninhabitable within decades due to climate change, *Nat. Sci. Rep., 5, 14546*, doi:10.1038/srep14546.
Storlazzi, C. D., S. B. Gingerich, A. van Dongeren, O. M. Cheriton, P. W. Swarzenski, E. Quataert, C. I. Voss, D. W. Field, H. Annamalai, G. A. Piniak, and R. McCall (2018), Most atolls will be uninhabitable by the mid-21st century because of sea-level rise exacerbating wave-driven flooding, *Science Advances, 4*, doi:10.1126/sciadv.aap9741.
Symonds, G., D. A. Huntley, and A. J. Bowen (1982), Two-dimensional surf beat: Long wave generation by a time-varying breakpoint, *J. Geophys. Res., 87(C1)*, 492–498, doi:10.1029/JC087iC01p00492.
Symonds, G., K. P. Black, and I. R. Young (1995), Wave-driven flow over shallow reefs. *J. Geophys. Res.*, 100, 2,639–2,648.
Thompson R. O. R. Y. (1979), Coherence significance levels, *J. of Atm. Sc.,* 36, 2020–2021.
Torres-Freyermuth, A., I. Marino-Tapia, C. Coronado, G. Medellin, A. Pedrozo-Acuna, R. Silva, J. Candela, and R. Iglesias-Prieto (2012), Modeling water levels in Puerto Morelos reef lagoon, *Nat. Hazards Earth Syst. Sci., 12*, 3765–3773, doi:10.5194/nhess-12-3765-2012.
van Dongeren, A., J. Battjes, T. Janssen, J. van Noorloos, K. Steenhauer, G. Steenbergen, and A. Reniers (2007), Shoaling and shoreline dissipation of low-frequency waves, *J. Geophys. Res., 112*, C02011, doi:10.1029/2006JC003701.
van Dongeren, A., R. Lowe, A. Pomeroy, D. M. Trang, D. Roelvink, G. Symonds, and R. Ranasinghe (2013), Numerical modeling of low frequency wave dynamics over a fringing coral reef, *Coastal Eng., 73*, 178–190, doi:10.1016/j.coastaleng.2012.11.004.
Vetter, O., J. M. Becker, M. A. Merrifield, A.C. Péquignet, J. Aucan, S. J. Boc, and C. E. Pollock (2010), Wave setup over a Pacific Island fringing reef, *J. Geophys. Res., 115, C12066*, doi:10.1029/2010JC006455.
Vila-Concejo, A., D. Harris, A. Shannon, J. Webster, and H. Power (2013), Coral reef sediment dynamics: evidence of sand-apron evolution on a daily and decadal scale, *J. Coastal Res., SI65*, 606–611, doi:10.2112/SI65-103.1
Yao, Y., Z. Huang, S. G. Monismith, and E. Y. M. Lo (2012), 1DH Boussinesq modeling of wave transformation over fringing reefs. *Oc. Eng., 47*, 30-42, doi:10.1016/j.oceaneng.2012.03.010.
Young, I. R. (1989), Wave transformation over coral reefs, *J. Geophys. Res., 94(C7)*, 9779–9789, doi:10.1029/JC094iC07p09779.

Table 1 – Summary of physical model experiment. H_s = significant wave height; T_p = peak wave period; h = water depth in the flume; h_{reef} is water depth across the reef platform; and D_{run} is run duration. Proto-type values are: H_s = 2, 3 and 4 m; T_p = 9.9 and 16.3 s; and h_{reef} = 0, 1 and 2 m.

Run#	H_s (m)	T_p (s)	h (m)	h_{reef} (m)	D_{run} (min)
Series A is low tide runs – reef platform only					
A1	0.04	1.4	0.47	0	12
A2	0.04	2.3	0.47	0	12
A3	0.06	1.4	0.47	0	12
A4	0.06	2.3	0.47	0	12
A5	0.08	1.4	0.47	0	12
A6	0.08	2.3	0.47	0	12
Series B is MSL runs – reef platform only					
B1	0.04	1.4	0.49	0.02	12
B2	0.04	2.3	0.49	0.02	12
B3	0.06	1.4	0.49	0.02	12
B4	0.06	2.3	0.49	0.02	12
B5	0.08	1.4	0.49	0.02	12
B6	0.08	2.3	0.49	0.02	12
Series C is high tide runs – reef platform only					
C1	0.04	1.4	0.51	0.04	12
C2	0.04	2.3	0.51	0.04	12
C3	0.06	1.4	0.51	0.04	12
C4	0.06	2.3	0.51	0.04	12
C5	0.08	1.4	0.51	0.04	12
C6	0.08	2.3	0.51	0.04	12
Series E is sea-level rise response runs – with reef island					
E1	0.06	1.4	0.51	0.04	30
E2	0.06	1.4	0.52	0.05	90
E3	0.06	1.4	0.53	0.06	90
E4	0.08	1.4	0.51	0.04	90
E5	0.08	1.4	0.52	0.05	90
E6	0.08	1.4	0.53	0.06	420

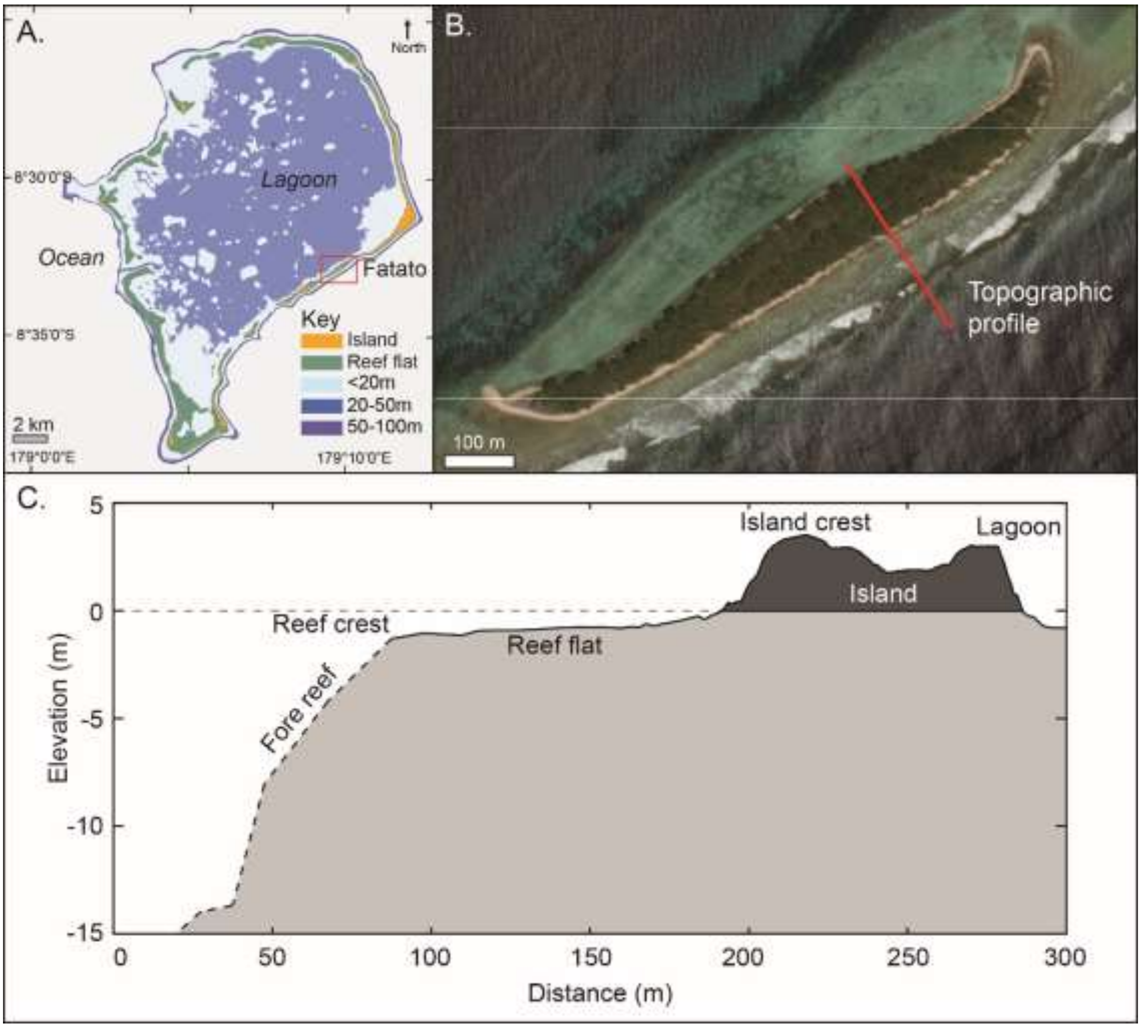

Figure 1 – (a) Geographical location of the gravel reef island of Fatato, Tuvalu, in the Pacific Ocean. (b) Aerial photograph of Fatato with the location of the topographic profile shown in (c). The dimensions and morphology of the coral reef platform and island in this paper are based on that of Fatato. Elevation is relative to mean sea level.

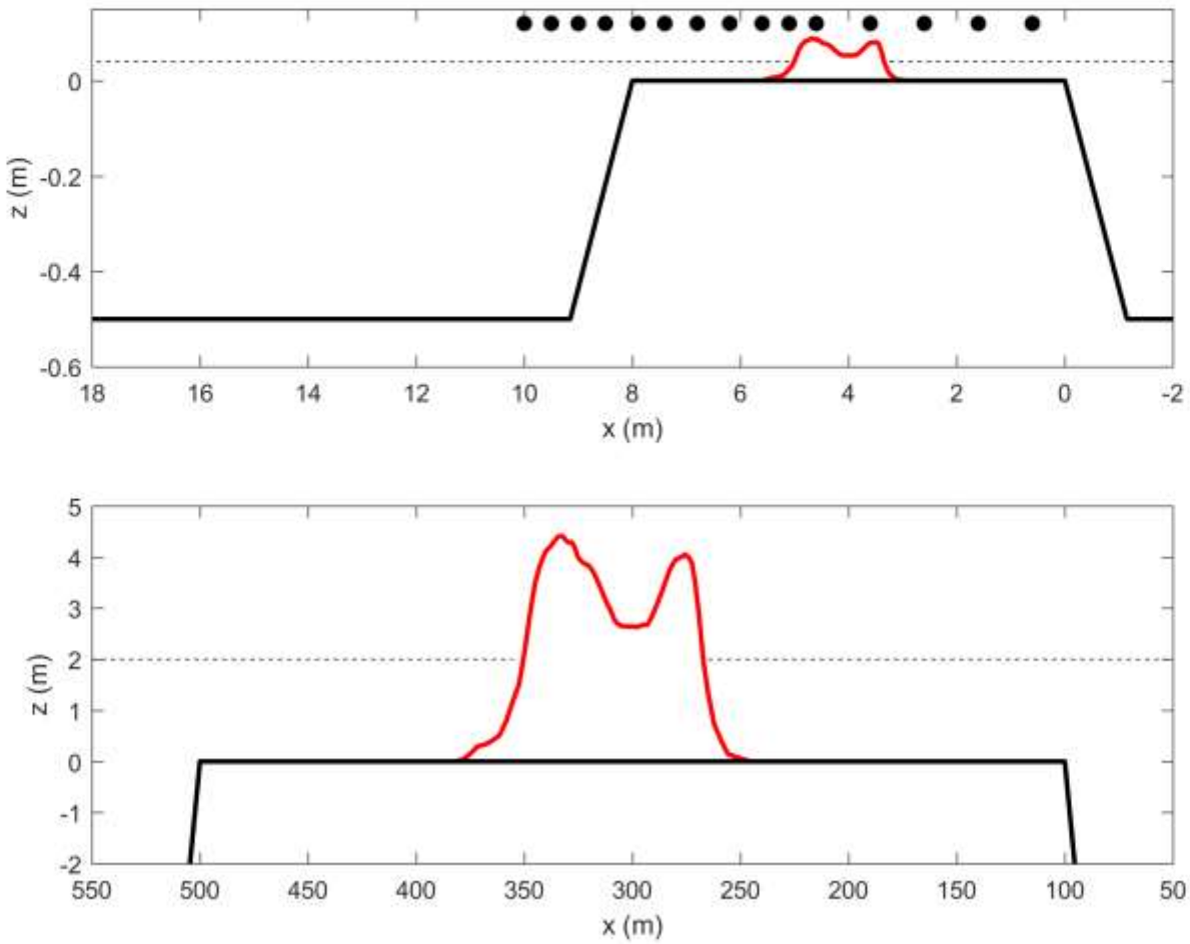

Figure 2 – Upper panel shows cross-section of reef platform and island for the 1:50 scale laboratory experiment. The wave paddle is located at *x* = 18 m; the wave gauges are indicated by the red circles and the mean high tide level is represented by the horizontal dashed line (0.04 m). Lower panel shows zoomed in section of the reef platform and island at the proto-type scale used for the XBeach numerical modelling. The offshore and onshore boundaries of the model are at *x* = -1000 m and *x* = 0 m, respectively, and the water depth away from the reef platform is 25 m.

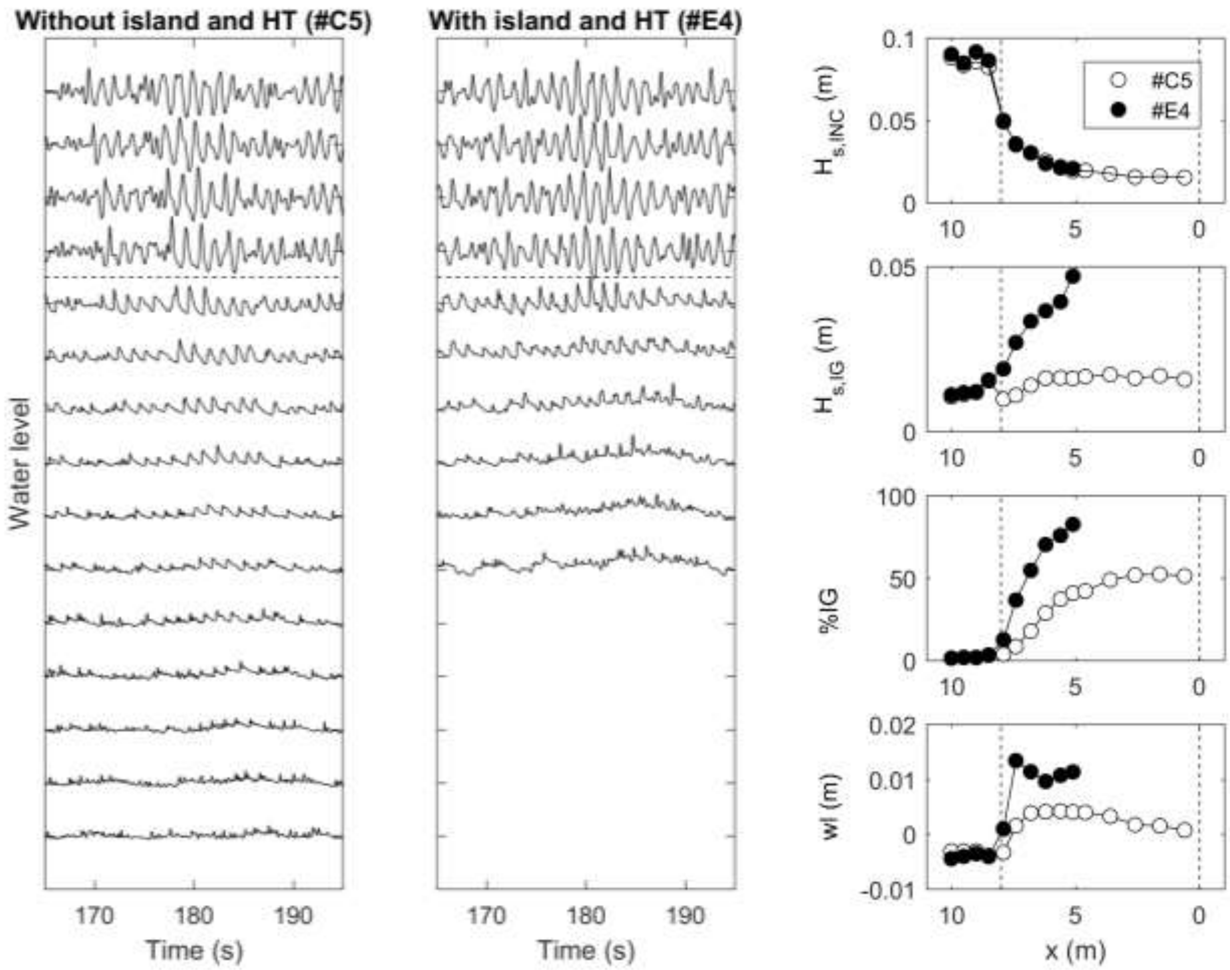

Figure 3 – Left and middle panel shows 30-s time series of water level for the 15 wave gauges during run #C5 (without island) and #E4 (with island), with conditions H_s = 0.08 m; T_p = 1.4 s; h_{reef} = 0.04 m. The time series are offset by 0.12 m and stacked from the seaward-most (top) to the landward-most (bottom) gauge. At each location, the plotted time series are relative to the local MSL (i.e., wave set-up removed), and the horizontal dashed line represents the seaward edge of the reef platform. Right panels shows 10-min across-reef summary statistics for run #C5 (white circles) and run #E4 (black circles) of, from top to bottom, significant incident wave height $H_{s,INC}$, significant infragravity wave height $H_{s,IG}$, percentage of infragravity wave energy *%IG* and mean water level *wl*. The vertical dashed lines represent the edges of the reef platform and the separation between incident and infragravity wave energy was at a frequency of 0.1 Hz.

789

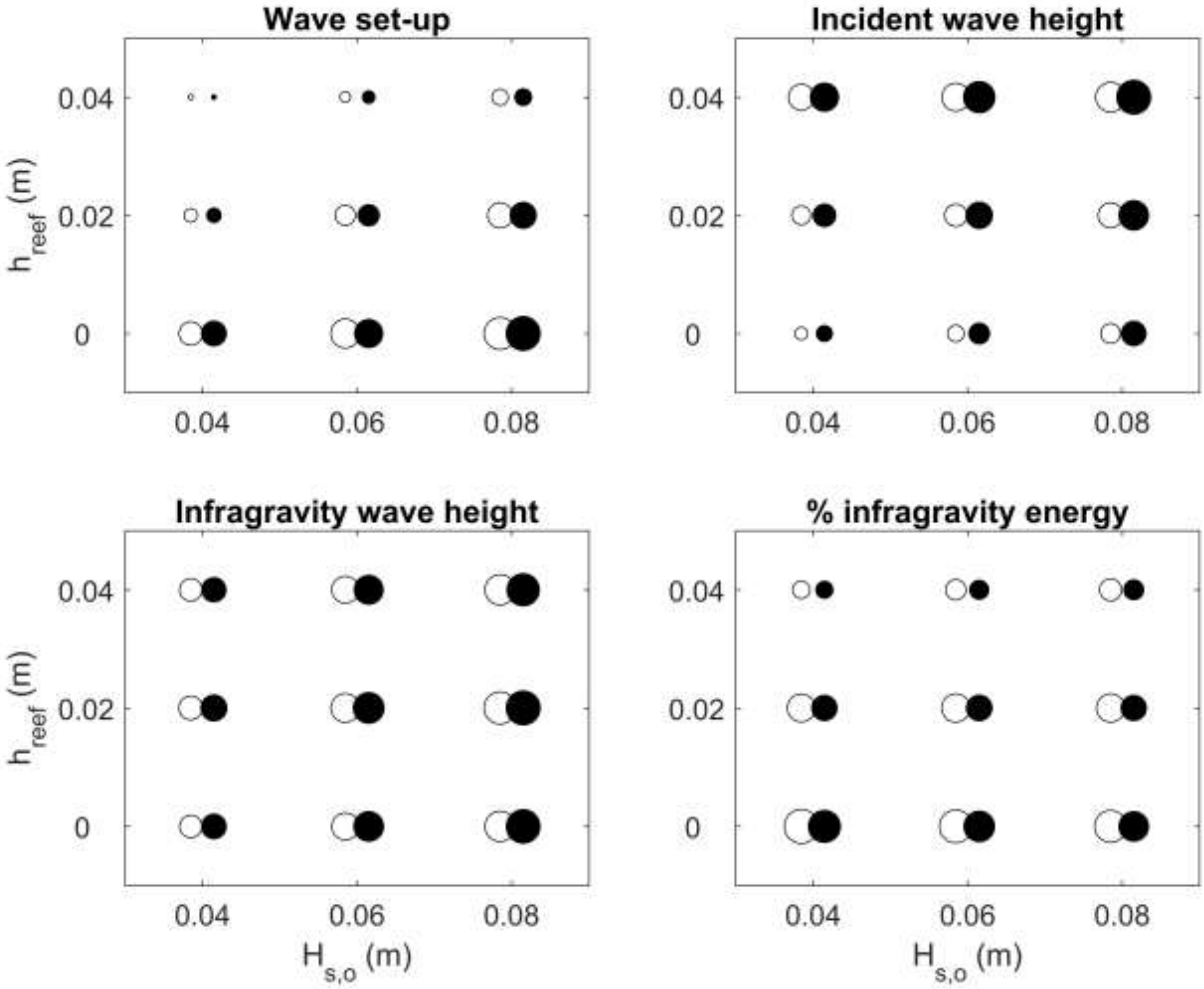

Figure 4 – Summary statistics for key hydrodynamic variables for all runs in Series A, B and C with values averaged across the middle of the reef platform, from *x* = 3.6–6.8 m (wave gauges 7–12). Data are plotted as a function of the (offshore) significant wave height $H_{s,o}$ and the water depth across the platform h_{reef} with the size of the circles scaled by the value of the parameter plotted. Maximum parameter values, representing maximum size of the symbols, are: wave set-up = 0.017 m; incident wave height = 0.029 m; infragravity wave height = 0.020 m; and % infragravity energy = 82%. White and black circles represent runs with peak wave period T_p of 1.4 and 2.3 s, respectively.

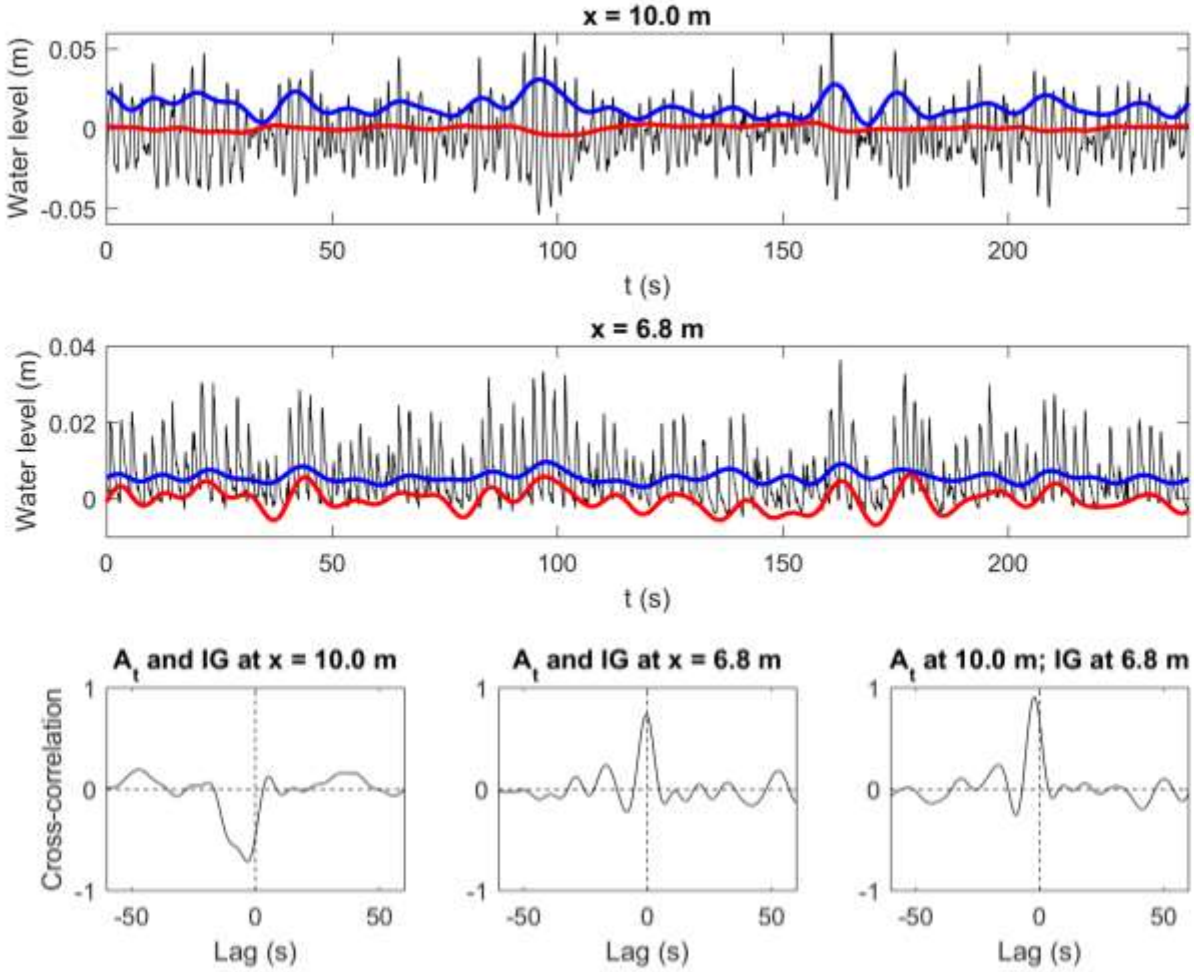

Figure 5 – Correlation between wave groupiness and IG wave motion. Two upper panels shows 4-min time series of η_t (thin black line), A_t (thick blue line) and $\eta_{t,IG}$ (thick red line) collected on the fore-reef (*x* = 10 m) and reef platform (*x* = 6.8 m) during run #B4. Three lower panels show the cross-correlation function between, from left to right, A_t and $\eta_{t,IG}$ at *x* = 10 m; A_t and $\eta_{t,IG}$ at *x* = 6.8 m; and A_t *x* = 10 m and $\eta_{t,IG}$ at *x* = 6.8 m.

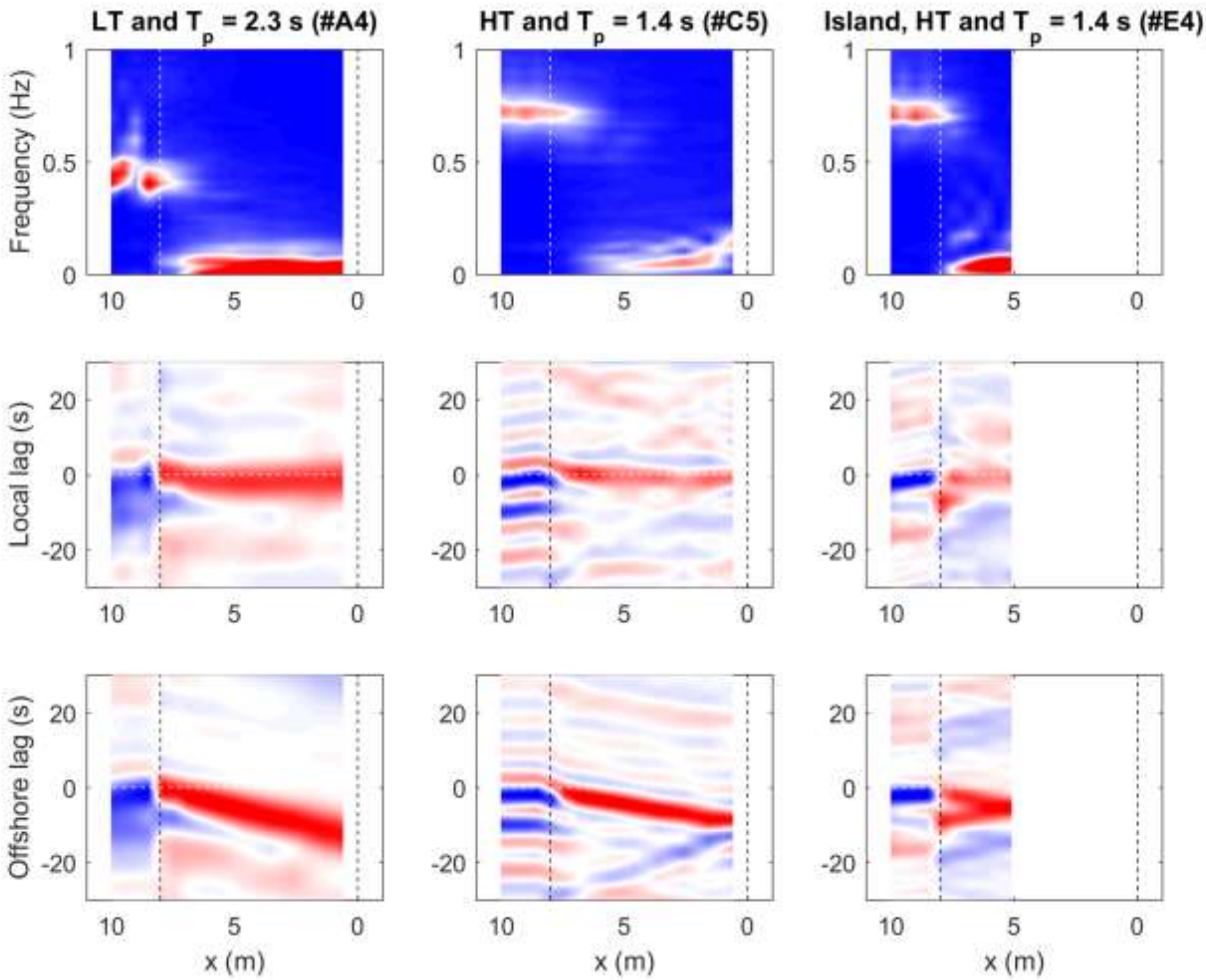

Figure 6 – Characteristics of the measured infragravity wave signal across the reef platform for run #A4 (without island, low tide and T_p = 2.3 s; left panels), run #C5 (without island, high tide and T_p = 1.4 s; middle panels) and run #E4 (with island, high tide and T_p = 1.4 s; right panels). Upper panels show the normalised wave spectrum (normalised by the total variance). Middle panels show the cross-correlation function between the lowpass-filtered wave envelope A_t and the infragravity wave signal $\eta_{t,IG}$ for each of the wave gauges (infragravity frequency cut-off = $1/(4T_p)$ Hz). Bottom panels show the cross-correlation function between A_t of the seaward-most wave gauge (x = 10 m) and $\eta_{t,IG}$ at each of the wave gauges. The vertical dashed lines in all panels represent the edges of the reef platform. The colour axis in the cross-correlation panels runs from -0.75 (dark blue) to 0.75 (dark red).

792

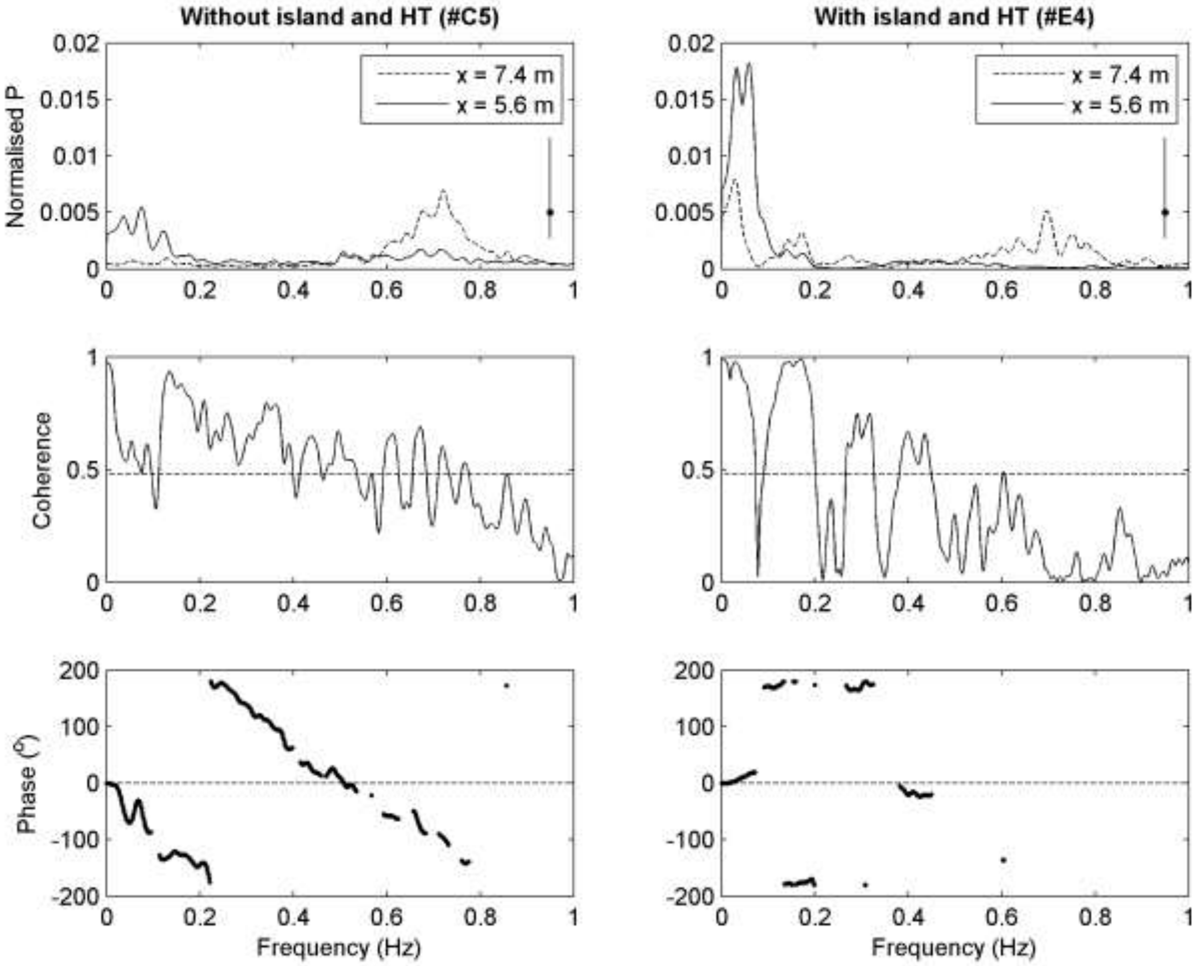

Figure 7 – Cross-spectral analysis between wave time series recorded at *x* = 7.4 m and *x* = 5.6 m for run C5 (without island; left panels) and for run E4 (with island; right panels). Top panels show normalised spectra (normalised by the total variance); middle panels show squared coherence spectra; and bottom panels show phase spectra. The spectra were computed for 16 degrees of freedom and the vertical line in the normalised spectra represent the 95% confidence levels of spectral estimates, while the horizontal dashed line in the squared coherence spectra shows the 1% significance level computed according to *Thompson* (1979). In the phase spectra only values are plotted for which the squared coherence exceeded the 1% significance level.

793

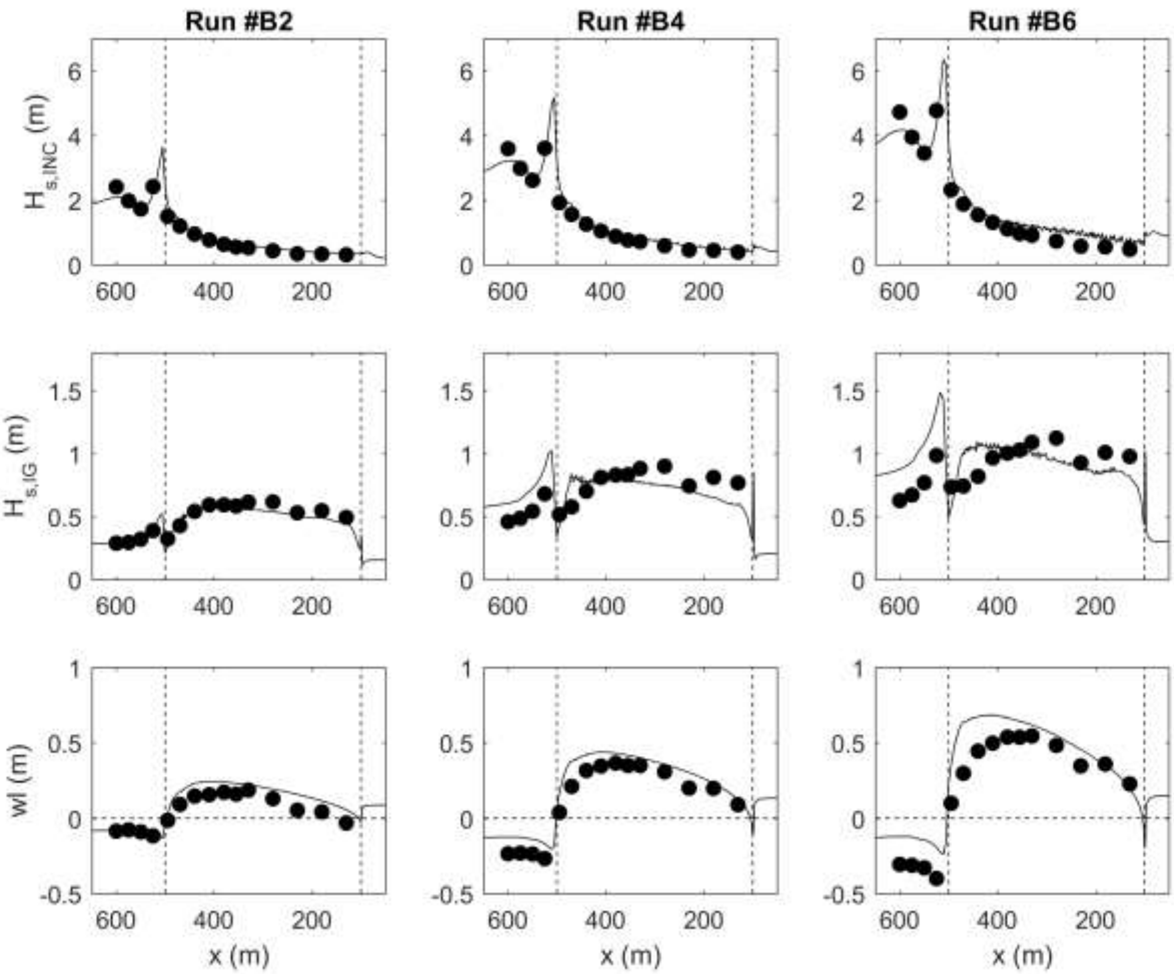

Figure 8 – Comparison of wave heights and water levels between small-scale physical model results (black circles) and proto-type XBeach modelling results (black solid line) for the long-period runs of Series B (mid-tide). From left to right, the results represent runs B2 ($H_{s,o}$ = 2 m), B4 ($H_{s,o}$ = 3 m) and B6 ($H_{s,o}$ = 4 m), and the following parameters are plotted from top to bottom: significant incident wave height $H_{s,INC}$, significant infragravity wave height $H_{s,IG}$, and mean water level *wl*. The vertical dashed lines represent the edges of the reef platform.

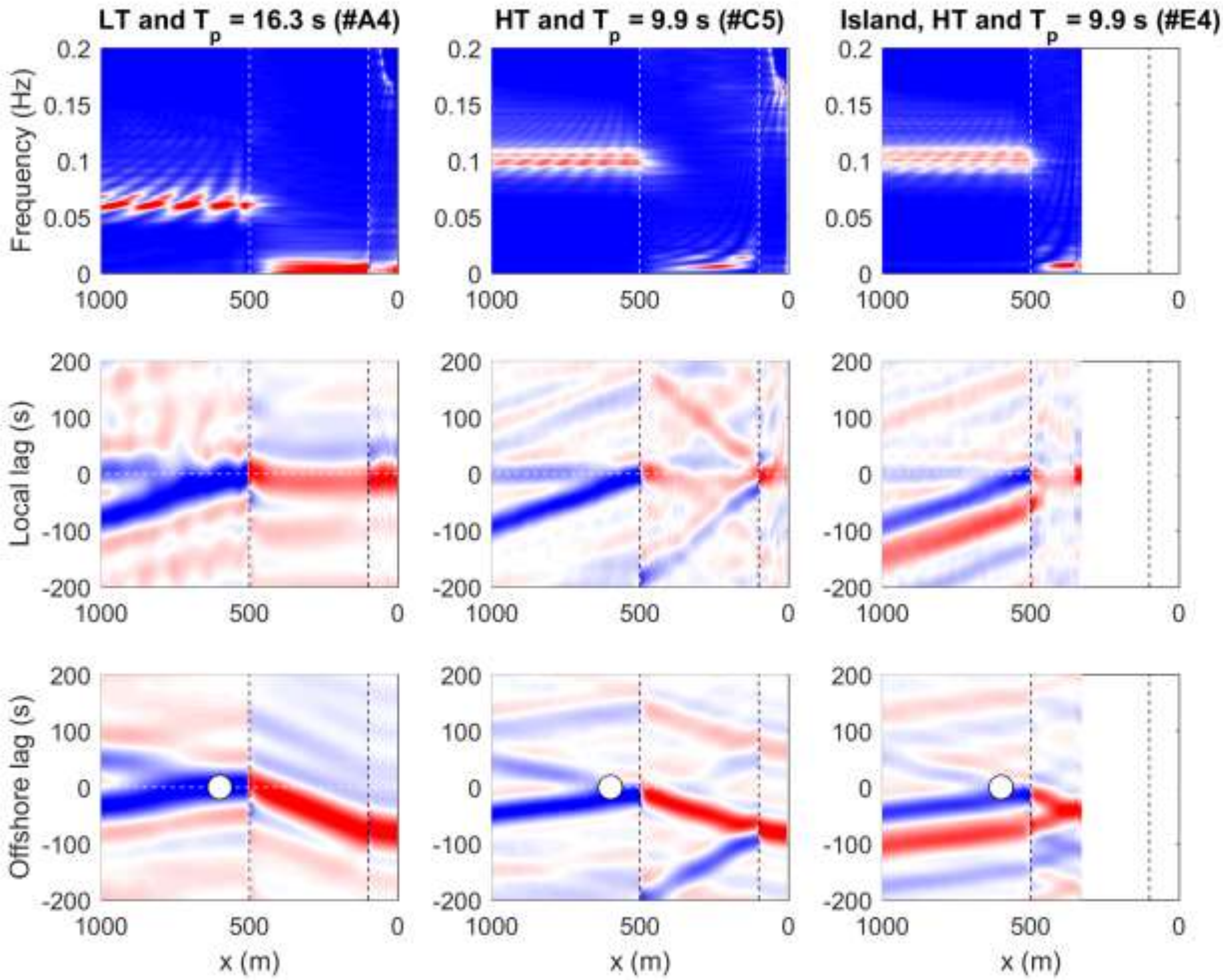

Figure 9 – Characteristics of the XBeach-modelled infragravity wave signal across the reef platform for run #A4 (without island, low tide and T_p = 16.3 s; left panels), run #C5 (without island, high tide and T_p = 9.9 s; middle panels) and run #E4 (with island, high tide and T_p = 9.9 s; right panels). Upper panels show the normalised wave spectrum. Middle panels show the cross-correlation function between the lowpass-filtered wave envelope A_t and the infragravity wave signal $\eta_{t,IG}$ for each of the wave gauges (infragravity frequency cut-off = $1/(4T_p)$ Hz). Bottom panels show the cross-correlation function between A_t at x = 600 m (marked with white circle) and $\eta_{t,IG}$ at each of the model grid points. The vertical dashed lines in all panels represent the edges of the reef platform. The colour axis in the cross-correlation panels run from -0.75 (dark blue) to 0.75 (dark red).

796

797

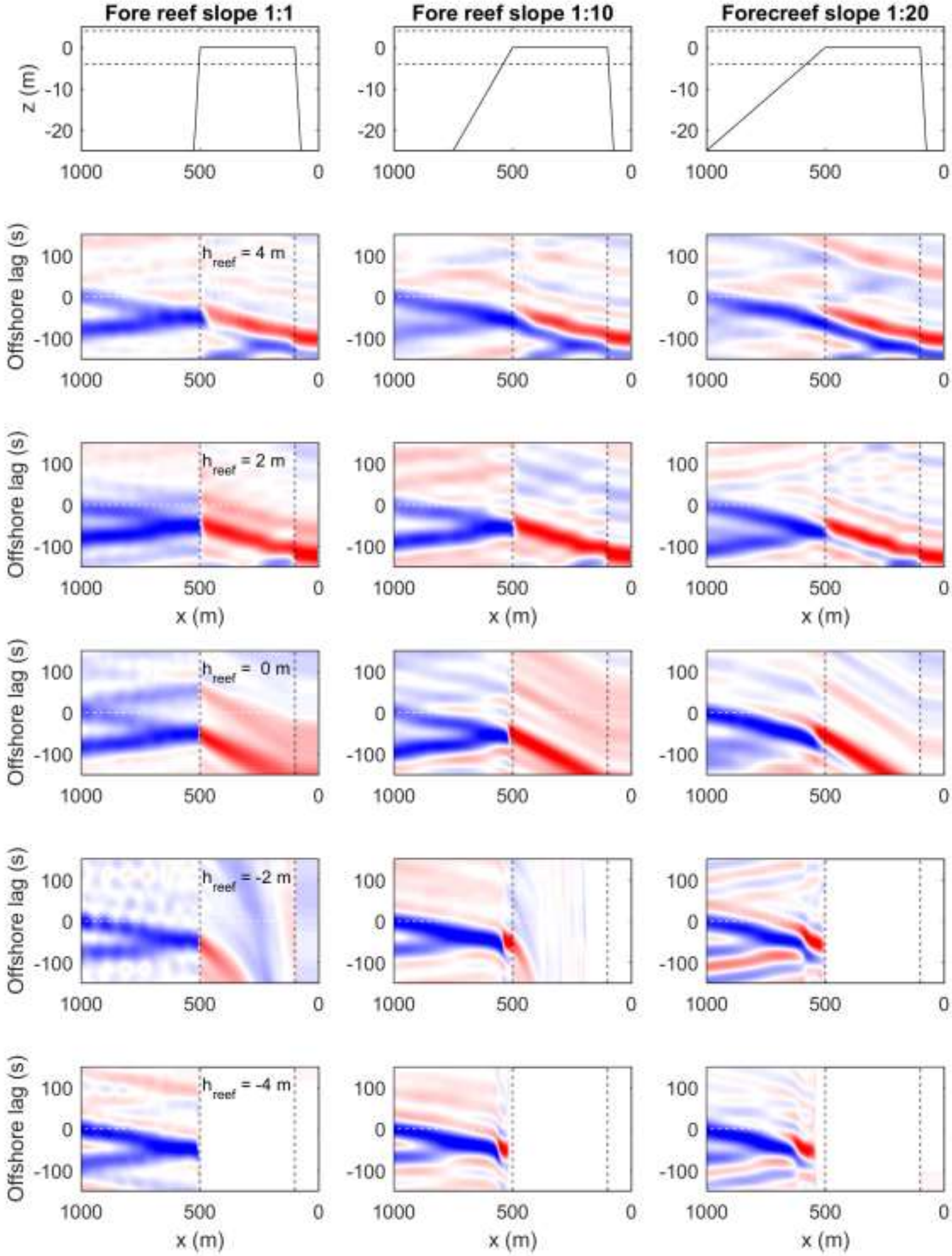

Figure 10 – Characteristics of the XBeach modelled infragravity wave signal for reef platforms with varying gradients of fore reef: 1:1 (left panels); 1:10 (middle panels) and 1:20 (right panels). Forcing conditions are $H_{s,o}$ = 2.5 m; T_p = 12.5 s; and h_{reef} varies, from top to bottom in 2-m increments, from 4 m (high tide + 2 m) to -4 m (low tide – 4 m). Upper panel shows reef morphology and the extreme water levels; all other panels show the cross-correlation function between the lowpass-filtered wave envelope A_t at the seaward model boundary (x = 1000 m) and the infragravity wave signal $\eta_{t,IG}$ at each of the model grid points for different water levels. The vertical dashed lines in all panels represent the edges of the reef platform. The colour axis in the cross-correlation panels runs from -1 to 1.

798

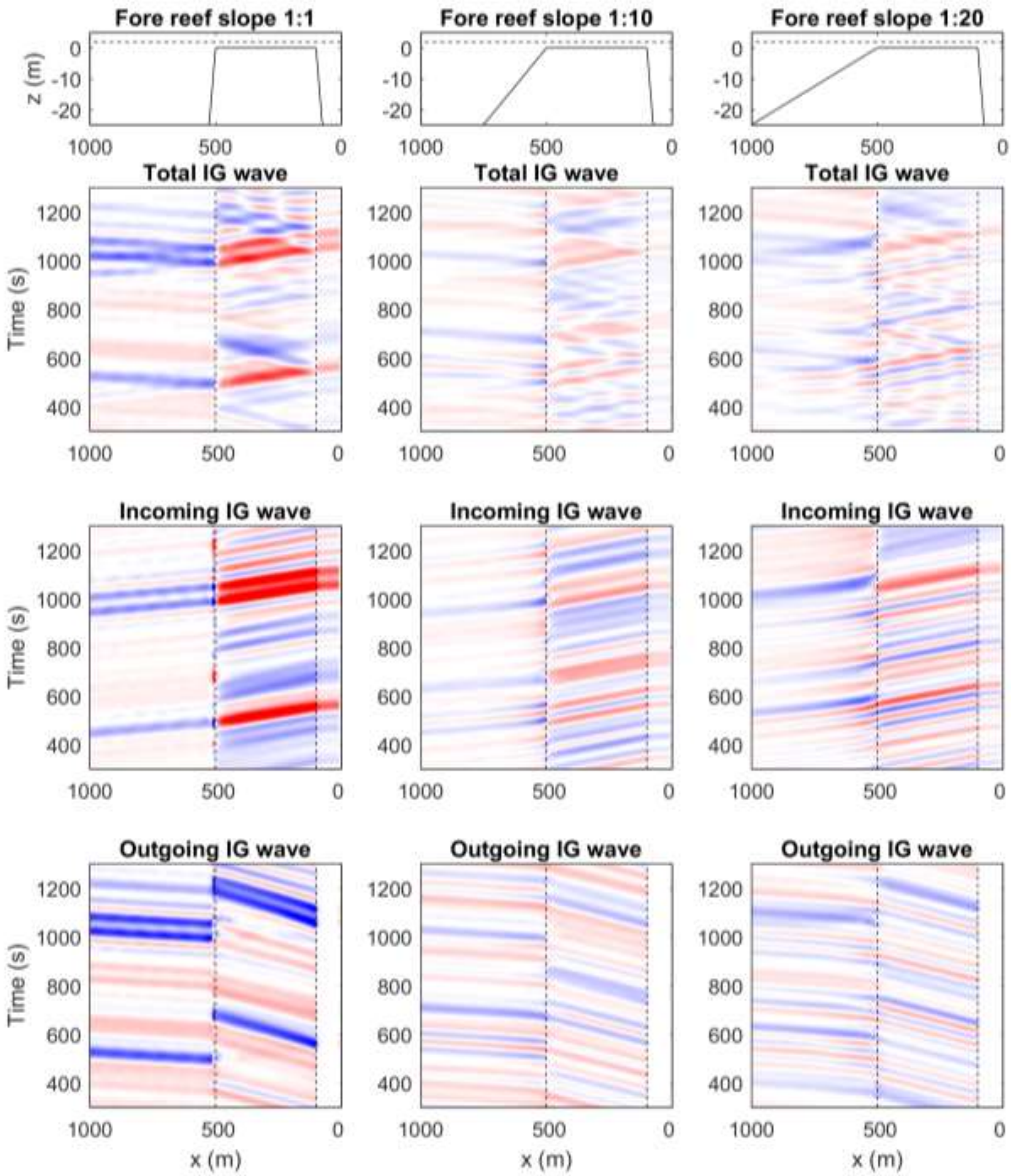

Figure 11 – Propagation of incoming and outgoing infragravity waves across the reef platform for fore reef slopes of 1:1 (left panels), 1:10 (middle panels) and 1:20 (right panels). Upper panels shows reef morphology for the three different fore reef slopes and the 2-m water level for which the wave transformation was modelled; other panels show the spatial-temporal evolution of, from top to bottom, the total, incoming and outgoing IG wave motion. The incoming and outgoing IG components of η_t were obtained using a lowpass filter of $4T_p$ and the method of *Guza et al.* (1984; Eqs 6 and 7). The vertical dashed lines in all panels represent the edges of the reef platform. The colour axis in the time series runs from -0.6 to 0.6 m; thus, dark blue and red 'stripes' represent IG wave troughs and crests, respectively.

799

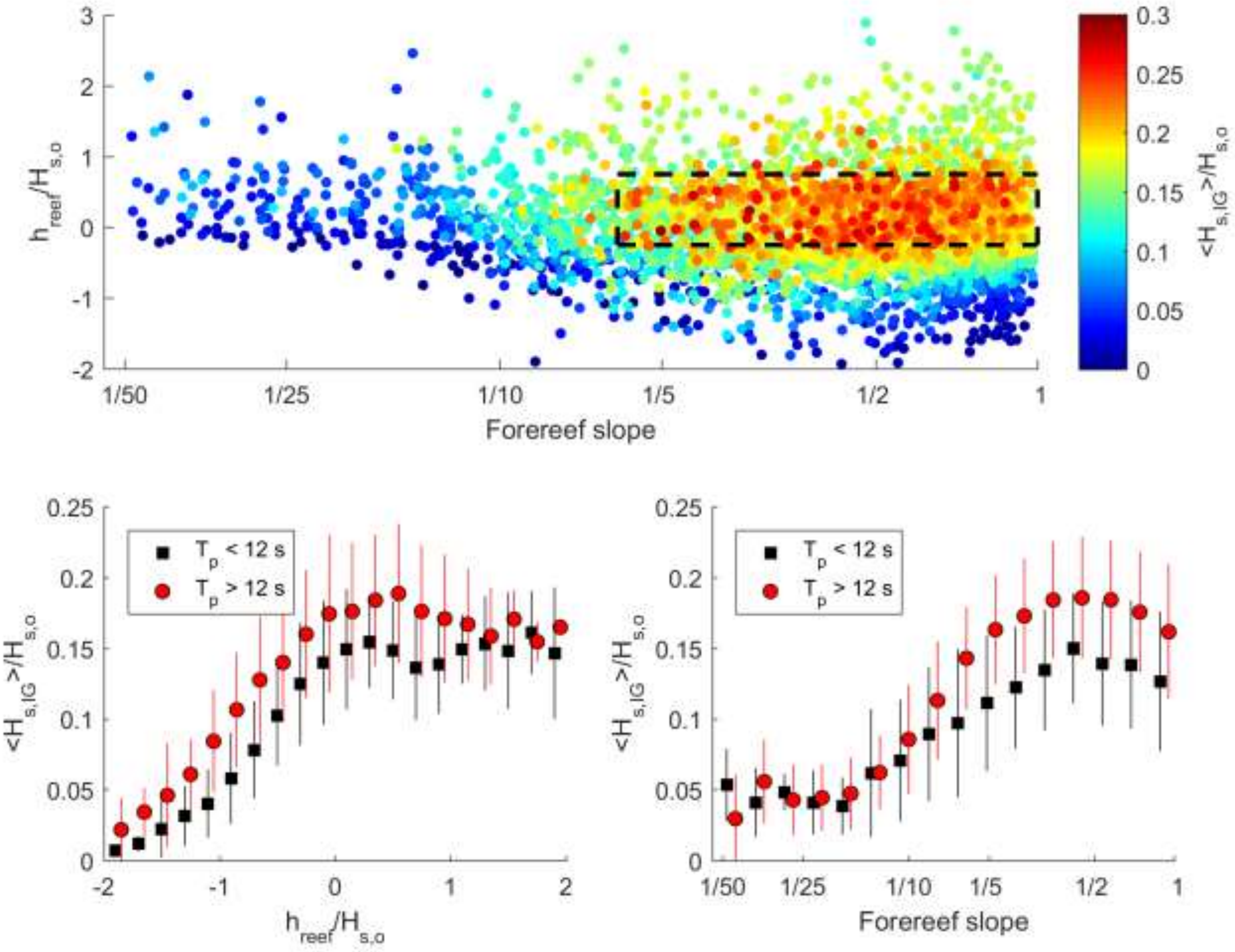

Figure 12 – Modelled characteristics of the infragravity wave signal averaged across the reef platform for c. 4000 XBeach runs with varying fore reef slopes, wave conditions and water levels. Upper panel shows the relative infragravity wave energy $<H_{s,IG}>/H_{s,o}$ (proportional to colour of symbols; see colour bar) averaged across the reef platform as a function of fore reef slope and relative water level $h_{reef}/H_{s,o}$. Lower-left and lower-right panels show mean and standard deviation associated with $H_{s,IG}/H_{s,o}$ computed for distinct bins of $h_{reef}/H_{s,o}$ and fore reef slope, respectively, divided into short- and long-period waves, using a peak period T_p of 12 s to separate the two groups of waves.

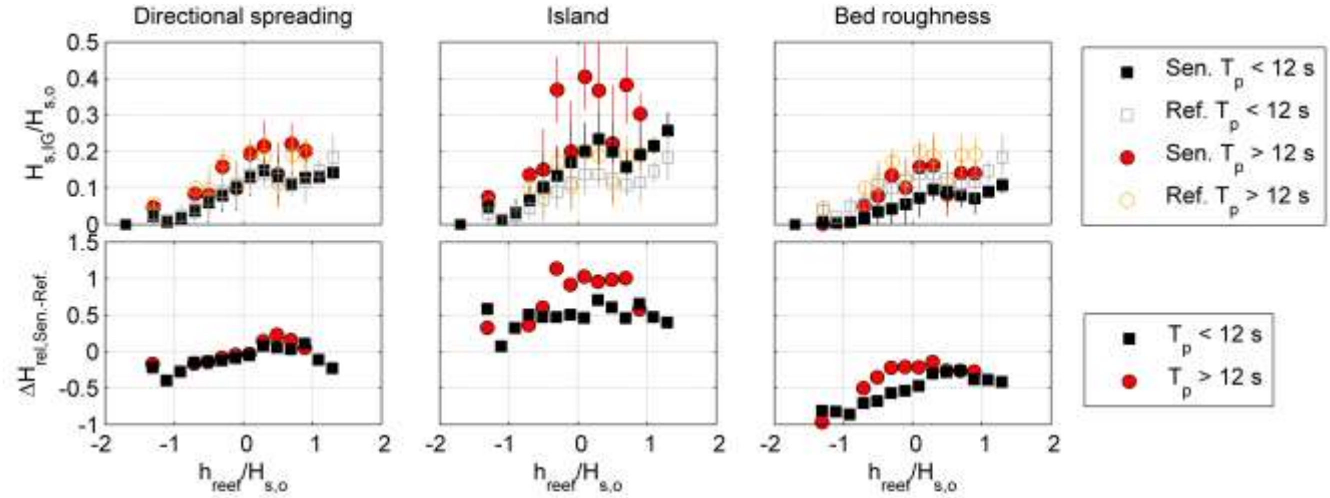

Figure 13 – Modelled characteristics of the infragravity wave signal averaged across the reef platform for three sensitivity analyses with 107 XBeach runs each. Left panels compare 2DH with 1D model simulations; middle panels compare model simulations with an without an island on the reef platform; and right panels compare low-roughness (c_f = 0.002) and high-roughness (c_f = 0.1) simulations. The upper panels show mean and standard deviation associated with $<H_{s,IG}>/H_{s,o}$ in sensitivity simulations (filled symbols; 'Sen') and equivalent reference simulations (open symbols; 'Ref') computed for distinct bins of $h_{reef}/H_{s,o}$ and divided into short- and long-period waves, using a peak period T_p of 12 s to separate the two groups of waves. The bottom panels show the relative difference in $<H_{s,IG}>/H_{s,o}$ between the sensitivity and reference simulations computed for distinct bins of $h_{reef}/H_{s,o}$. Note that due to the fact that only a subsection of all the 1D simulations was carried out in the sensitivity simulations, not all $h_{reef}/H_{o,s}$ bins contain comparative data.